# On the energy decomposition in variational phase-field models for brittle fracture under multi-axial stress states

F Vicentini, C Zolesi, P Carrara, C Maurini, L de Lorenzis

# On the energy decomposition in variational phase-field models for brittle fracture under multi-axial stress states

F. Vicentini[a,*], C. Zolesi[b,*], P. Carrara[a], C. Maurini[b,**], L. De Lorenzis[a]

[a] *Computational Mechanics Group, Eidgenössische Technische Hochschule Zürich, Tannenstrasse 3, 8092 Zürich, Switzerland*
[b] *CNRS, Institut Jean Le Rond d'Alembert, Sorbonne Université, UMR 7190, 75005, Paris, France*

**Abstract**

Phase-field models of brittle fracture are typically endowed with a decomposition of the elastic strain energy density in order to realistically describe fracture under multi-axial stress states. In this contribution, we identify the essential requirements for this decomposition to correctly describe both nucleation and propagation of cracks. Discussing the evolution of the elastic domains in the strain and stress spaces as damage evolves, we highlight the links between the nucleation and propagation conditions and the modulation of the elastic energy with the phase-field variable. In light of the identified requirements, we review some of the existing energy decompositions, showcasing their merits and limitations, and conclude that none of them is able to fulfil all requirements. As a partial remedy to this outcome, we propose a new energy decomposition, denoted as star-convex model, which involves a minimal modification of the volumetric-deviatoric decomposition. Predictions of the star-convex model are compared with those of the existing models with different numerical tests encompassing both nucleation and propagation.

*Keywords:* Nucleation, Propagation, Fracture, Multi-axial, Phase-field

## 1. Introduction

Francfort and Marigo revisited Griffith's criterion from a variational perspective by casting it into a global energy minimization framework; thus, they formulated a general principle circumventing the need for ad-hoc criteria to handle arbitrarily complex crack topologies in 2D or 3D [1]. The direct application of the ensuing (so-called *sharp-crack*) model is limited by the difficulty to handle displacement jumps in the numerical setting. Phase-field approaches come into play as a regularization of the sharp-crack model [2, 3] and offer a smeared description of the crack as the localization of an auxiliary variable, i.e., the phase-field variable. The regularized model is prone to a simple numerical treatment using standard finite element discretizations with smooth basis functions; it introduces a regularization length $\ell$, which defines the typical width of the localization bands representing the approximation of the cracks.

Although originally developed to describe crack *propagation*, phase-field models are naturally able to predict the evolution of damage from a pristine material, which can be regarded as the capability to predict *nucleation* of cracks. From a theoretical perspective, this ability can be justified by treating the auxiliary regularization variable as a *damage* variable and interpreting the model as a gradient damage model endowed with a finite internal length $\ell$ [4]. Gradient damage modeling in the quasi-static rate-independent setting defines the system evolution through the three principles of *stability*, *irreversibility* and *energy balance* [5]. In particular, the stability requirement is equivalent to *local* energy minimization, in contrast to the starting sharp-crack problem which instead calls for *global* energy minimization. Evolution following local energy minima is not only numerically convenient when dealing with large-scale problems, but also more physically reasonable as it does not require crossing energy barriers [6–8].

Following the three principles of gradient damage model evolution, localization of damage naturally occurs upon the loss of stability of the homogeneous solution whose threshold depends on the length $\ell$ [4]. Thus, the internal

*These authors contributed equally.
**Corresponding author, corrado.maurini@sorbonne-universite.fr.

length can be tuned to calibrate the uniaxial tensile strength of the material [9, 10]. On the other hand, once the elastic parameters, the fracture toughness of the material and $\ell$ are fixed, the standard phase-field model does not offer any additional degree of freedom to calibrate the strength related to scenarios different from uniaxial tension, such as the compressive strength or the shear strength, see the discussion in [11, 12]. Flexibility in defining the strength envelope represents the main problem of *nucleation* under multi-axial stress states. As for crack *propagation* under such stress states, the most relevant problem is to model unilateral contact appropriately [13].

There is a wealth of literature proposing phase-field models for brittle fracture under multi-axial stress states. The performance of these models is demonstrated through different examples, making their comparison not immediate and their strength and limitations not obvious. Among these contributions, some preserve a variational nature; the most popular variational solutions [13, 14] are based on elastic energy decompositions. This idea is adopted in [12, 15–17], justified through structured deformation theory. Other contributions are inspired by anisotropic materials [18–20], propose cohesive fracture [21], introduce plasticity [22–24] or propose an explicit treatment of the crack direction [25–27]. Unfortunately, the available variational models implicitly prioritize either nucleation or propagation, and (as we will show in this paper, at least for the most popular ones) none of them can describe both aspects correctly without introducing excessive complexity with respect to the original model or moving away from the framework of linear elastic (brittle) materials. Other models step outside the variational framework; in this way, they more easily achieve the needed flexibility to handle nucleation and propagation, but only at the cost of giving up the theoretical and practical advantages of the variational structure [11, 28–32]. The variational principle naturally comes with a simple stability concept and it allows the use of the mathematical tools of calculus of variations to discuss the existence of solutions and to study the asymptotic $\Gamma$-convergence behavior. Additionally, the finite element tangent stiffness matrix stemming from a variational formulation is automatically symmetric, which gives important advantages in numerics. Moreover, the Drucker-Prager Ilyushin postulate is satisfied only if the damage criterion is derived from a variational formulation where the strain work is a state function [33] and the thermodynamic consistency of non-variational models is not granted.

To date, a study that highlights advantages and drawbacks of different energy decompositions based on a consistent set of criteria and common examples is still lacking. In this contribution, we first define these criteria; subsequently, we perform a systematic review of some available models, highlighting their performance in relation to the defined criteria. We find out that none of the examined energy decompositions is able to satisfy all the proposed criteria, as they perform well with respect to either nucleation or propagation of cracks. As a remedy, we propose a new model, which we denote as *star-convex model*; this model is still based on an energy decomposition, but it is specifically designed to satisfy the desired requirements for both nucleation and propagation.

The paper is structured as follows. Section 2 offers a brief review on the basic ingredients of standard phase-field modeling of brittle fracture, shows its limitations and formulates the requirements for an ideal model to describe fracture under multi-axial stress states. In light of the defined requirements, Section 3 reports a review of some of the available models, all based on decompositions of the elastic strain energy density. In Section 4, the novel star-convex model is introduced. Section 5 is dedicated to numerical experiments that showcase the advantages and limitations of the models previously illustrated, including the new one. The main conclusions are drawn in Section 6.

As follows, we summarize the notation and some useful relations. Vectors and second-order tensors will be both denoted by boldface fonts, e.g. $\boldsymbol{u}$ and $\boldsymbol{\sigma}$ for the displacement vector and stress tensor, respectively. For the standard orthogonal decomposition of second-order tensors in volumetric and deviatoric parts we will use the following notation (exemplified on $\boldsymbol{\sigma}$)

$$\boldsymbol{\sigma} = \boldsymbol{\sigma}_{\mathrm{vol}} + \boldsymbol{\sigma}_{\mathrm{dev}}, \qquad \boldsymbol{\sigma}_{\mathrm{vol}} = \frac{\mathrm{tr}(\boldsymbol{\sigma})}{n}\mathbf{I}, \qquad \boldsymbol{\sigma}_{\mathrm{dev}} = \boldsymbol{\sigma} - \frac{\mathrm{tr}(\boldsymbol{\sigma})}{n}\mathbf{I}, \qquad \boldsymbol{\sigma}_{\mathrm{vol}} \cdot \boldsymbol{\sigma}_{\mathrm{dev}} = 0,$$

where $\mathbf{I}$ is the second-order identity tensor and $n$ is the number of space dimensions. For an isotropic elastic undamaged material with Young's modulus $E_0$ and Poisson's ratio $\nu_0$, we denote by $(\lambda_0, \mu_0, \kappa_0)$ the Lamé and the bulk moduli given by:

$$\lambda_0 = \frac{E_0\nu_0}{(1+\nu_0)[1-(n-1)\nu_0]}, \qquad \mu_0 = \frac{E_0}{2(1+\nu_0)}, \qquad \kappa_0 = \lambda_0 + \frac{2\mu_0}{n} = \frac{E_0}{n[1-(n-1)\nu_0]}.$$

Given a scalar valued function: $f : x \to f(x) \in \mathbb{R}$, we define its positive part and negative part as:

$$\langle f(x)\rangle_+ = \frac{f(x)}{2} + \frac{|f(x)|}{2}, \qquad \langle f(x)\rangle_+ = \frac{f(x)}{2} - \frac{|f(x)|}{2}.$$

## 2. Standard model and ideal model requirements

In this section, we first introduce the general formulation of a phase-field model for brittle fracture. We then proceed to specialize this framework to the case of the standard model. Subsequently, we clarify the limitations of this model and leverage these insights to define the ideal requirements for a model able to handle fracture under multi-axial stress state.

### *2.1. General formulation*

Let us consider a homogeneous body occupying the domain $\Omega \subset \mathbb{R}^n$. Its current state at point $\boldsymbol{x} \in \Omega$ is described by the displacement field $\boldsymbol{u}(\boldsymbol{x})$ and the irreversible scalar damage field $\alpha(\boldsymbol{x}) \in [0, 1]$, with $\alpha = 0$ and $\alpha = 1$ denoting a pristine and a fully damaged material, respectively. The *strain energy density* is a differentiable function of the strain, the damage and the damage gradient

$$W(\boldsymbol{\varepsilon}, \alpha, \nabla\alpha) := \varphi(\boldsymbol{\varepsilon}, \alpha) + w_1 \left( w(\alpha) + \ell^2 |\nabla\alpha|^2 \right), \tag{1}$$

where the first term $\varphi$ is the *elastic strain energy density* and the second term is the *dissipated energy density*. The elastic strain energy density is convex and positively homogeneous of degree 2 with respect to $\boldsymbol{\varepsilon}$ at fixed $\alpha$, i.e. $\varphi(r\boldsymbol{\varepsilon}, \alpha) = r^2\varphi(\boldsymbol{\varepsilon}, \alpha)\ \forall r \geq 0$, and it decreases with respect to $\alpha$ at fixed $\boldsymbol{\varepsilon}$. The dissipated energy density is composed of a local and a non-local part. The local term $w_1 w(\alpha)$ corresponds to the amount of energy dissipated per unit volume to damage homogeneously a pristine material; the *dissipation function* $w(\alpha)$ is a non-negative increasing function of $\alpha$ such that $w(0) = 0$ and $w(1) = 1$, and we refer to $w_1$ as the *specific fracture energy*. The non-local term is assumed to be a quadratic function of the gradient of the damage, whereby $\ell$ is an *internal length*.

The *total energy* at time $t$, $\mathcal{E}_t(\boldsymbol{u}, \alpha)$, is the sum of the strain energy and the potential energy of the external forces:

$$\mathcal{E}_t(\boldsymbol{u}, \alpha) := \int_\Omega W(\boldsymbol{\varepsilon}(\boldsymbol{u}), \alpha, \nabla\alpha) \mathrm{d}\Omega - \int_\Omega \boldsymbol{b}_t \cdot \boldsymbol{u} \mathrm{d}\Omega - \int_{\partial_N\Omega} \boldsymbol{f}_t \cdot \boldsymbol{u} \mathrm{d}\Omega, \tag{2}$$

where $\boldsymbol{b}_t$ is the body force defined in $\Omega$ and $\boldsymbol{f}_t$ is the surface traction applied on $\partial_N\Omega$, both at time $t$, and $\boldsymbol{\varepsilon}(\boldsymbol{u}) := \mathrm{sym}(\nabla\boldsymbol{u})$ is the linear strain tensor. The applied displacement $\bar{\boldsymbol{u}}_t$ is applied on the complementary part of the boundary $\partial_D\Omega$.

In the time-discrete setting of the evolution problem, given $\alpha_p$ (the damage at the previous time $t_p$), the displacement and the damage field at time $t = t_p + \Delta t$ are found by solving the minimization problem:

$$(\boldsymbol{u}, \alpha) = \underset{(\hat{\boldsymbol{u}}, \hat{\alpha}) \in C_t \times \mathcal{D}(\alpha_p)}{\arg\,\mathrm{loc}\,\min}\ \mathcal{E}_t(\hat{\boldsymbol{u}}, \hat{\alpha}), \tag{3}$$

where

$$C_t := \{\boldsymbol{u} \in H^1(\Omega; \mathbb{R}^n) : \boldsymbol{u} = \bar{\boldsymbol{u}}_t \text{ on } \partial_D\Omega\}, \quad \mathcal{D}(\alpha_p) := \{\alpha \in H^1(\Omega) : \alpha \geq \alpha_p\} \tag{4}$$

are the spaces of the admissible displacement and damage fields at time $t$ from the previous state with damage $\alpha_p$. Equation (3) requires $(\boldsymbol{u}, \alpha)$ to satisfy:

$$\begin{aligned} &\forall (\hat{\boldsymbol{u}}, \hat{\alpha}) \in C_t \times \mathcal{D}(\alpha_p),\ \exists \bar{h} > 0 : \forall h \in [0, \bar{h}] \\ &\mathcal{E}_t(\boldsymbol{u} + h(\boldsymbol{u} - \hat{\boldsymbol{u}}), \alpha + h(\alpha - \hat{\alpha})) - \mathcal{E}_t(\boldsymbol{u}, \alpha) \geq 0. \end{aligned} \tag{5}$$

A necessary condition for this local constrained minimization is found taking into account only the first-order expansion of the energy increment:

$$\mathcal{E}_t'(\boldsymbol{u}, \alpha)(\boldsymbol{u} - \hat{\boldsymbol{u}}, \alpha - \hat{\alpha}) \geq 0, \qquad \forall (\hat{\boldsymbol{u}}, \hat{\alpha}), \tag{6}$$

where

$$\mathcal{E}_t'(\boldsymbol{u}, \alpha)(\boldsymbol{v}, \beta) := \frac{d}{dh} \mathcal{E}_t(\boldsymbol{u} + h\boldsymbol{v}, \alpha + h\beta) \bigg|_{h=0} \tag{7}$$

is the *Gateaux* derivative of the functional $\mathcal{E}_t(\boldsymbol{u}, \alpha)$ in the direction $(\boldsymbol{v}, \beta)$. For smooth solutions, we can show with standard arguments of Calculus of Variation that the first-order optimality condition (6) is equivalent to the *equilibrium equation* and boundary conditions

$$\mathrm{div}\boldsymbol{\sigma}(\boldsymbol{\varepsilon}, \alpha) + \boldsymbol{b}_t = \mathbf{0} \text{ in } \Omega, \qquad \boldsymbol{\sigma}(\boldsymbol{\varepsilon}, \alpha) \cdot \mathbf{n} = \boldsymbol{f}_t \text{ on } \partial_N \Omega \tag{8}$$

and to the Karush-Kuhn-Tucker (KKT) conditions and boundary conditions

$$\begin{array}{lll} -Y(\boldsymbol{\varepsilon}, \alpha) + w_1 w'(\alpha) - 2\ell^2 w_1 \Delta\alpha \geq 0, & \alpha - \alpha_p \geq 0, & (-Y(\boldsymbol{\varepsilon}, \alpha) + w_1 w'(\alpha) - 2\ell^2 w_1 \Delta\alpha)(\alpha - \alpha_p) = 0 \quad \text{on } \Omega, \\ \nabla\alpha \cdot \mathbf{n} \geq 0, & \alpha - \alpha_p \geq 0, & (\nabla\alpha \cdot \mathbf{n})(\alpha - \alpha_p) = 0 \qquad \text{on } \partial\Omega, \end{array} \tag{9}$$

where $\mathbf{n}$ is the outer unit normal to the boundary, We denote the KKT conditions as *damage criterion*, *irreversibility* and *loading-unloading condition*, respectively. The conjugate quantities

$$\boldsymbol{\sigma}(\boldsymbol{\varepsilon}, \alpha) := \frac{\partial \varphi(\boldsymbol{\varepsilon}, \alpha)}{\partial \boldsymbol{\varepsilon}}, \qquad Y(\boldsymbol{\varepsilon}, \alpha) := -\frac{\partial \varphi(\boldsymbol{\varepsilon}, \alpha)}{\partial \alpha} \tag{10}$$

are the *stress* tensor and the *damage energy release rate*, respectively.

A crucial notion for the following analysis of damage under multi-axial stress states is that of *elastic domains*. In the context of local damage modeling, these are the sets in which stresses and strains must remain in order for the material to follow a linearly elastic behavior without damage evolution, i.e., $\alpha = \alpha_p$. In our non-local context, their boundaries define the elastic limits for materials with homogeneous damage distribution ($\Delta\alpha = 0$). The elastic domains in the strain space $\mathcal{R}(\alpha)$ and in the stress space $\mathcal{R}^*(\alpha)$ are defined as the sets

$$\mathcal{R}(\alpha) := \left\{ \boldsymbol{\varepsilon} \in \mathrm{Sym} : -\frac{\partial \varphi(\boldsymbol{\varepsilon}, \alpha)}{\partial \alpha} \leq w_1 w'(\alpha) \right\}, \tag{11}$$

$$\mathcal{R}^*(\alpha) := \left\{ \boldsymbol{\sigma} \in \mathrm{Sym} : \frac{\partial \varphi^*(\boldsymbol{\sigma}, \alpha)}{\partial \alpha} \leq w_1 w'(\alpha) \right\}, \tag{12}$$

where Sym denotes the space of symmetric tensors and $\varphi^*(\boldsymbol{\sigma}, \alpha)$ is the *complementary energy density* defined as

$$\varphi^*(\boldsymbol{\sigma}, \alpha) := \sup_{\hat{\boldsymbol{\varepsilon}} \in \mathrm{Sym}} \boldsymbol{\sigma} \cdot \hat{\boldsymbol{\varepsilon}} - \varphi(\hat{\boldsymbol{\varepsilon}}, \alpha). \tag{13}$$

At a given value of $\alpha \in [0, 1)$ a damage model enjoys the *strain-hardening* property if, $\forall \beta > \alpha$, $\mathcal{R}(\beta) \supset \mathcal{R}(\alpha)$. and the *stress-softening* property if $\mathcal{R}^*(\beta) \subset \mathcal{R}^*(\alpha)$, see [34]. The strain-hardening property is important to ensure the uniqueness of the solution for the damage at a given strain upon damage evolution, while the stress-softening property is fundamental to allow for damage localization [34].

### *2.2. The standard phase-field model*

For the model that we refer to in the following as the *standard* phase-field model, the elastic strain energy density is defined as

$$\varphi(\boldsymbol{\varepsilon}, \alpha) = a(\alpha)\varphi_0(\boldsymbol{\varepsilon}) \qquad \text{with} \qquad \varphi_0(\boldsymbol{\varepsilon}) = \frac{\kappa_0}{2}\mathrm{tr}^2(\boldsymbol{\varepsilon}) + \mu_0 |\boldsymbol{\varepsilon}_{\mathrm{dev}}|^2, \tag{14}$$

where $\varphi_0$ is the elastic strain energy density for a homogeneous isotropic linear elastic material and $a(\alpha)$ is the degradation function. This function describes the degradation of the linear elastic properties with damage; it is a decreasing function of $\alpha$ going from $a(0) = 1$ to $a(1) = 0$. By Legendre transformation, the complementary energy density $\varphi^*(\boldsymbol{\sigma}, \alpha)$ is derived as

$$\varphi^*(\boldsymbol{\sigma}, \alpha) = s(\alpha)\varphi_0^*(\boldsymbol{\sigma}) \quad \text{with} \quad \varphi_0^*(\boldsymbol{\sigma}) = \frac{\mathrm{tr}^2(\boldsymbol{\sigma})}{2n^2\kappa_0} + \frac{|\boldsymbol{\sigma}_{\mathrm{dev}}|^2}{4\mu_0} \quad \text{and} \quad s(\alpha) := \frac{1}{a(\alpha)}. \tag{15}$$

Combining (11-15) we obtain

$$\mathcal{R}(\alpha) := \left\{ \boldsymbol{\varepsilon} \in \mathrm{Sym} : \frac{\kappa_0}{2}\mathrm{tr}^2(\boldsymbol{\varepsilon}) + \mu_0 |\boldsymbol{\varepsilon}_{\mathrm{dev}}|^2 \leq -\frac{w_1 w'(\alpha)}{a'(\alpha)} \right\}, \tag{16}$$

$$\mathcal{R}^*(\alpha) := \left\{ \boldsymbol{\sigma} \in \mathrm{Sym} : \frac{\mathrm{tr}^2(\boldsymbol{\sigma})}{2n^2\kappa_0} + \frac{|\boldsymbol{\sigma}_{\mathrm{dev}}|^2}{4\mu_0} \leq \frac{w_1 w'(\alpha)}{s'(\alpha)} \right\}. \tag{17}$$

The expressions of the elastic strain energy density in (14) and of the complementary energy density in (15) ensure that the transformation of spaces $\mathcal{R}(\alpha)$ and $\mathcal{R}^*(\alpha)$ with varying $\alpha$ is a homothety centered in $\boldsymbol{\varepsilon} = \mathbf{0}$ and $\boldsymbol{\sigma} = \mathbf{0}$, respectively.

The selection of the degradation function $a(\alpha)$ and of the dissipation function $w(\alpha)$ has a significant impact on the description of the damaging behavior. Two classical expressions are

$$\mathrm{AT}_1 : \quad a(\alpha) = (1-\alpha)^2, \quad w(\alpha) = \alpha, \quad \alpha_{\mathrm{peak}} = 0, \tag{18}$$

$$\mathrm{AT}_2 : \quad a(\alpha) = (1-\alpha)^2, \quad w(\alpha) = \alpha^2, \quad \alpha_{\mathrm{peak}} = \frac{1}{4}. \tag{19}$$

These two models are both strain-hardening $\forall \alpha \in [0,1]$, and stress-softening $\forall \alpha \in [\alpha_{\mathrm{peak}}, 1]$, whereas they are stress-hardening $\forall \alpha \in [0, \alpha_{\mathrm{peak}})$. These properties hold regardless of the loading direction due to the homothetic evolution of $\mathcal{R}(\alpha)$ and $\mathcal{R}^*(\alpha)$ with $\alpha$. The primary difference between $\mathrm{AT}_1$ and $\mathrm{AT}_2$ is that $\mathrm{AT}_1$ displays a linearly elastic behavior up to a non-zero elastic limit stress, whereas $\mathrm{AT}_2$ features a zero elastic limit stress, therefore with $\mathrm{AT}_2$ an infinitesimal load is sufficient to trigger the onset of damage.

For $\mathrm{AT}_1$ and $\mathrm{AT}_2$ applied to the 1D bar under tensile loading it is shown in [4, 35] that, for sufficiently long bars ($L \gg \ell$), the damage localization in bands (crack nucleation) occurs at the level of damage at which the behavior of the model changes from stress hardening to stress softening, i.e., at $\alpha = \alpha_{\mathrm{peak}}$. For $\mathrm{AT}_1$ this transition corresponds to the elastic limit because $\alpha_{\mathrm{peak}} = 0$. Under multi-axial loading, in [36] it is also shown that with the AT1 model and for a sufficiently large structure the transition from a stress-hardening to a stress-softening phase is a necessary and sufficient condition for the damage localization in bands (or cracks). For different types of phase-field models, these conclusions do not necessarily hold and a more careful study would be necessary, see [36, 37] for more details.

From now on, we focus only on $\mathrm{AT}_1$-like models ($w(\alpha) = \alpha$). Accordingly, we define the strength surface $\mathcal{S}^*$ as the set of stresses at the elastic limit, i.e., all stresses at the boundary of the elastic domain $\mathcal{R}^*(\alpha)$ for $\alpha = \alpha_{\mathrm{peak}} = 0$:

$$\mathcal{S}^* := \partial\mathcal{R}^*(0) = \left\{ \boldsymbol{\sigma} \in \mathrm{Sym} : \frac{\mathrm{tr}^2(\boldsymbol{\sigma})}{2n^2\kappa_0} + \frac{|\boldsymbol{\sigma}_{\mathrm{dev}}|^2}{4\mu_0} = \frac{w_1 w'(0)}{s'(0)} \right\}. \tag{20}$$

From $\mathcal{S}^*$, one can define the tensile and compressive strengths, $\sigma_e^+$ and $\sigma_e^-$, as the maximum and minimal allowable stress $\sigma$ for the uniaxial stress state $\boldsymbol{\sigma} = \sigma \boldsymbol{e}_1 \otimes \boldsymbol{e}_1$, and the shear strength $\tau_e$ as the maximum allowable stress $\tau$ for stress states of pure shear $\boldsymbol{\sigma} = \tau \boldsymbol{e}_1 \otimes \boldsymbol{e}_2$. For the standard model, these quantities are given by

$$\sigma_e^+ := \sqrt{\frac{2E_0 w_1 w'(0)}{s'(0)}}, \qquad \tau_e := \sqrt{\frac{2\mu_0 w_1 w'(0)}{s'(0)}}, \qquad \sigma_e^- := -\sqrt{\frac{2E_0 w_1 w'(0)}{s'(0)}}. \tag{21}$$

In the setting of a 1D bar under tensile loading, the dissipated energy associated to the phase-field smeared representation of a crack is regarded as the dissipation upon rupture and is denoted as *fracture toughness* $G_c$. In [4, 35], the 1D localized damage distribution is derived analytically and the fracture toughness is accordingly expressed as

$$G_c = 4 w_1 \ell \int_0^1 \sqrt{w(\beta)}\, d\beta, \tag{22}$$

which for $\mathrm{AT}_1$ gives

$$G_c = \frac{8}{3} w_1 \ell. \tag{23}$$

Thus, from the experimental determination of $G_c$ and $\sigma_e^+$, it is possible to calibrate $w_1$ and $\ell$. In this sense, the regularization length can be viewed as a material property. In Figure 1, we plot the evolution of the elastic domains $\mathcal{R}(\alpha)$ and $\mathcal{R}^*(\alpha)$ with increasing $\alpha$ in both the volumetric-deviatoric plane (Figure 1a) and the plane spanned by the principal strain/stress components under the plane-strain assumption (Figure 1b). Given the symmetry of $\mathcal{R}(\alpha)$ and $\mathcal{R}^*(\alpha)$ with respect to the volumetric axis in Figure 1a and with respect to the bisector of the first and third quadrants in Figure 1b, we plot only half of $\mathcal{R}(\alpha)$ (in blue) and half of $\mathcal{R}^*(\alpha)$ (in red).

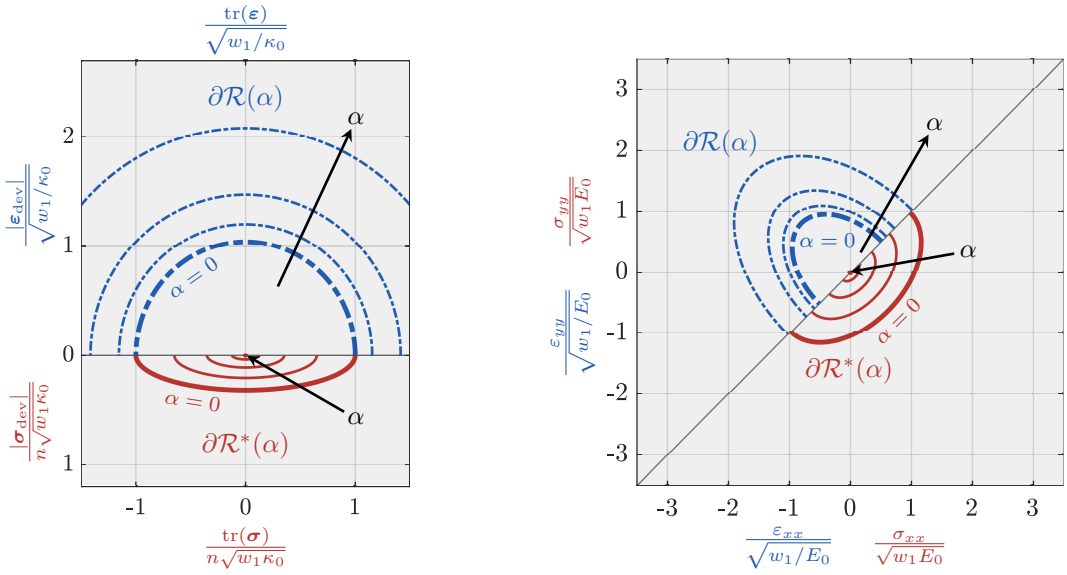


(a) (b)

Fig. 1: Elastic domains for the standard model in the strain (blue dash-dotted line) and stress (red solid line) space for $\alpha = \{0, 0.25, 0.5, 0.75, 1\}$ ($\nu_0 = 0.3$). The domains for $\alpha = 0$ (thick lines) are the nucleation domains (or strength surfaces). Volumetric-deviatoric diagram (a). Principal components diagram under the plane-strain assumption (b).

### *2.3. Limitations of the standard model*

The standard phase-field model has major limitations when considering multi-axial stress states. Regarding nucleation, we mention two limits evident from the shape of the elastic domains at $\alpha = 0$ (Figure 1):

- **Tension/compression symmetry**: Both $\mathcal{R}(0)$ and $\mathcal{R}^*(0)$ are ellipsoids in the strain and the stress spaces, respectively. As a consequence, the tensile and compressive strengths have the same magnitude. This is unrealistic for the majority of brittle materials, which typically feature a compressive strength one order of magnitude higher than the tensile strength. Moreover, the shear strength often increases with volumetric compression.

- **Lack of flexibility**: Assuming the elastic constants $\kappa_0$, $\mu_0$, the tensile strength $\sigma_e^+$ and the fracture toughness $G_c$ to be known, it is possible to calibrate $w_1$ and $\ell$ using (21) and (22). In this manner, all the model parameters are determined, thus the shape and size of the ellipsoids $\mathcal{R}(0)$ and $\mathcal{R}^*(0)$ are also fixed and it is not possible to match e.g. experimentally known values of $\sigma_e^-$ and/or $\tau_e$. This aspect is what we term lack of *flexibility* of the model.

Regarding propagation, we report a major limit related to the local behavior for $\alpha = 1$:

- **Zero residual stress**: In the standard model, the whole elastic strain energy drives the damage evolution. The consequence is that, once the maximum damage $\alpha = 1$ is locally reached, the elastic strain energy density vanishes regardless of the loading direction and the elastic domain in the stress space collapses to the point $\boldsymbol{\sigma} = \mathbf{0}$ (Figure 1). From now on, we denote the stress obtained for $\alpha = 1$

$$\boldsymbol{\sigma}_R(\boldsymbol{\varepsilon}) := \boldsymbol{\sigma}(\boldsymbol{\varepsilon}, 1) = \frac{\partial\varphi(\boldsymbol{\varepsilon}, 1)}{\partial\boldsymbol{\varepsilon}} \tag{24}$$

  as *residual stress*. Thus, for the standard model it is $\boldsymbol{\sigma}_R = \mathbf{0}$. This correctly avoids the transmission of tensile tractions across the crack boundary in mode 1 (opening), mode 2 and 3 (shear). However, it also gives zero tractions under compressive loading, thus it cannot properly represent unilateral contact at the crack faces. Determining the threshold that defines which load directions should be associated with zero residual stress and which should not to best model unilateral contact is a nontrivial task. In [38], it is shown that a zero residual

stress for $\mathrm{tr}(\boldsymbol{\varepsilon}) \geq 0$ and a residual elastic energy density which depends solely on the negative volumetric energy density (e.g., $\varphi(\boldsymbol{\varepsilon}, 1) = \frac{1}{2}\,\kappa_0\,\langle \mathrm{tr}(\boldsymbol{\varepsilon})\rangle_-^2$) can be used to approximate the non-interpenetration constraint in the sense of $\Gamma$-convergence.

### *2.4. Requirements to an ideal model*

In light of the previous observations on the standard model, we can now define the requirements for an ideal model as follows:

- **Strain-hardening**: As previously mentioned, this is a key requirement to ensure the uniqueness of the solution for the damage at a given strain upon damage evolution.
- **Stress-softening**: It is fundamental to allow for the presence of solutions with localised damage and hence for crack nucleation.
- **Tension/compression asymmetry**: At least we require that $|\sigma_e^-| > \sigma_e^+$. For some materials it would be ideal to have a shear strength that increases with volumetric compression.
- **Flexibility**: The model should contain enough parameters to allow for calibration of $\tau_e$ and $\sigma_e^-$ (or at least one of the two) independently of $\sigma_e^+$ (for given elastic properties and $G_c$).
- **Crack-like residual stress**: The ideal model does not transmit stress through the crack faces in the opening and shear modes but exhibits a compressive residual stress. Hinging on the consistent variational framework in [38], we require the presence of nonzero residual stresses exclusively for $\mathrm{tr}(\boldsymbol{\varepsilon}) < 0$. Accordingly, an elastic energy density such that $\varphi(\boldsymbol{\varepsilon}, 1) \propto \langle \mathrm{tr}(\boldsymbol{\varepsilon})\rangle_-^2$ fulfills the requirement.

Several models have been proposed in the literature to solve the limitations of the standard model under multi-axial stress states. In the following, we analyze some of these models in light of the requirements listed above.

## 3. Available variational phase-field models for multi-axial stress states

In this section, we review the main available variational phase-field models for multi-axial stress states. The advantages and limitations of these models in relation to the requirements listed in Section 2.4 are then exemplified through numerical experiments in Section 5. The models are all based on the following decomposition of the elastic strain energy (also denoted as energy split)

$$\varphi(\boldsymbol{\varepsilon}, \alpha) = a(\alpha)\varphi_D(\boldsymbol{\varepsilon}) + \varphi_R(\boldsymbol{\varepsilon}) \qquad \text{with} \qquad \varphi_D(\boldsymbol{\varepsilon}) + \varphi_R(\boldsymbol{\varepsilon}) = \varphi_0(\boldsymbol{\varepsilon}), \tag{25}$$

where $\varphi_D(\boldsymbol{\varepsilon})$ and $\varphi_R(\boldsymbol{\varepsilon})$ are respectively the *degradable* and the *residual* components of the elastic strain energy density. These components are non-negative and only vanish for $\boldsymbol{\varepsilon} = 0$; their sum yields the elastic energy density of a pristine material $\varphi_0(\boldsymbol{\varepsilon})$, defined as in (14). The idea behind this decomposition is that only certain modes of deformation contribute to the driving force for the nucleation and evolution of damage. Residual stresses at full damage are given by

$$\boldsymbol{\sigma}_R(\boldsymbol{\varepsilon}) = \boldsymbol{\sigma}(\boldsymbol{\varepsilon}, 1) = \frac{\partial \varphi_R(\boldsymbol{\varepsilon})}{\partial \boldsymbol{\varepsilon}}. \tag{26}$$

Only $\varphi_D(\boldsymbol{\varepsilon})$ contributes to the energy release rate $Y(\boldsymbol{\varepsilon}, \alpha)$; accordingly, it is the only component which affects the elastic domains

$$\mathcal{R}(\alpha) := \left\{ \boldsymbol{\varepsilon} \in \mathrm{Sym} : \varphi_D(\boldsymbol{\varepsilon}) \leq -\frac{w_1 w'(\alpha)}{a'(\alpha)} \right\}, \tag{27}$$

$$\mathcal{R}^*(\alpha) := \left\{ \boldsymbol{\sigma} \in \mathrm{Sym} : \varphi_D(\boldsymbol{\varepsilon}(\boldsymbol{\sigma}, \alpha)) \leq -\frac{w_1 w'(\alpha)}{a'(\alpha)} \right\}, \tag{28}$$

where $\boldsymbol{\varepsilon}(\boldsymbol{\sigma}, \alpha)$ is computed as the inverse of the constitutive law in (10). The choice of the decomposition strongly affects the evolution of the elastic domain and thus the predicted crack nucleation and propagation behavior under multi-axial stress states. Note that formulating the decomposition in the form of (25) ensures that $\mathcal{R}(\alpha)$ evolves with $\alpha$ as a simple homothety centered in the origin. Unlike in the case of the standard model, this is not always guaranteed for $\mathcal{R}^*(\alpha)$.

### 3.1. The volumetric-deviatoric split

The split proposed by Amor et al. [13] is based on the decomposition of the elastic strain energy density into a deviatoric and a volumetric part:

$$\varphi_D(\boldsymbol{\varepsilon}) = \frac{1}{2}\kappa_0 \langle \mathrm{tr}(\boldsymbol{\varepsilon})\rangle_+^2 + \mu_0 |\boldsymbol{\varepsilon}_{\mathrm{dev}}|^2, \qquad \varphi_R(\boldsymbol{\varepsilon}) = \frac{1}{2}\kappa_0 \langle \mathrm{tr}(\boldsymbol{\varepsilon})\rangle_-^2 \tag{29}$$

leading to the residual stresses

$$\boldsymbol{\sigma}_R(\boldsymbol{\varepsilon}) = \kappa_0 \langle \mathrm{tr}(\boldsymbol{\varepsilon})\rangle_- \mathbf{I}. \tag{30}$$

This model was constructed to recover unilateral contact conditions under compression. Indeed, in [38] it is demonstrated that the volumetric-deviatoric decomposition can be used to approximate the non-interpenetration constraint in the sense of Γ-convergence without affecting the tensile and shear behavior in the presence of a crack. The elastic domains are given in Appendix A.1 and illustrated in Figure 2. In this case, both domains evolve with $\alpha$ as homotheties centered in the origin.

This split introduces the desired asymmetry in tension and compression, as shown in Table 1, without adding residual stresses for $\mathrm{tr}(\boldsymbol{\varepsilon}) > 0$. However, it gives no flexibility in the choice of the shear strength, which is the same as in the standard model, nor in the compressive strength.

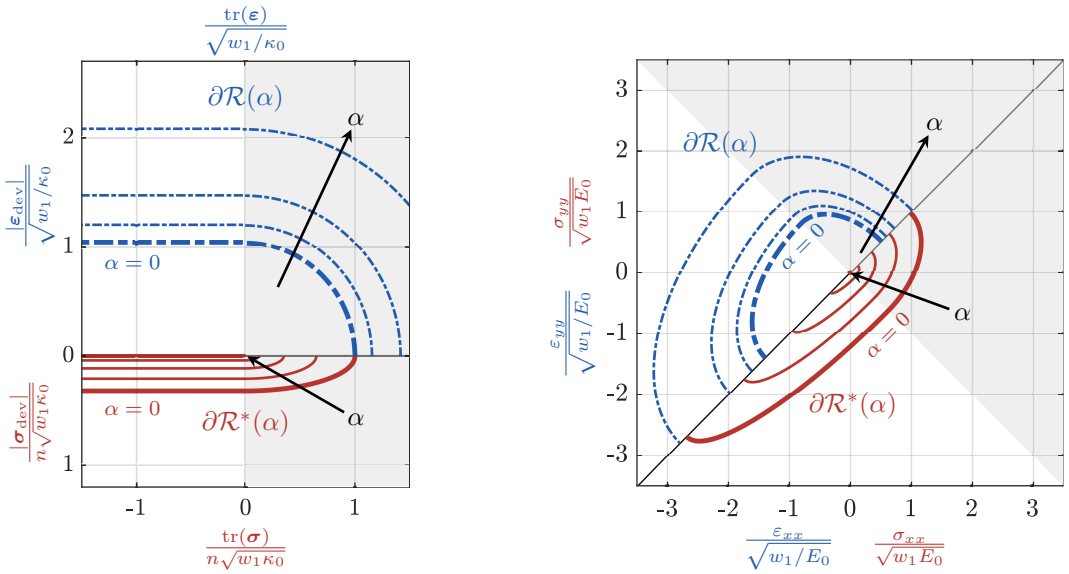


Fig. 2: Elastic domains for the model with volumetric-deviatoric split in the strain (blue dash-dotted line) and stress (red solid line) space for $\alpha = \{0, 0.25, 0.5, 0.75, 1\}$ ($\nu_0 = 0.3$). The domains for $\alpha = 0$ are the nucleation domains (or strength surfaces). The grey background indicates the parts of the elastic domains shared with the standard model. Volumetric-deviatoric diagram (a). Principal components diagram under the plane-strain assumption (b).

### 3.2. The spectral split

The decomposition introduced by Miehe et al. [14] is based on the eigenvalues and eigenvectors of the strain tensor

$$\varphi_D(\boldsymbol{\varepsilon}) = \frac{1}{2}\lambda_0 \langle \mathrm{tr}(\boldsymbol{\varepsilon})\rangle_+^2 + \mu_0 \boldsymbol{\varepsilon}^+ \cdot \boldsymbol{\varepsilon}^+, \qquad \varphi_R(\boldsymbol{\varepsilon}) = \frac{1}{2}\lambda_0 \langle \mathrm{tr}(\boldsymbol{\varepsilon})\rangle_-^2 + \mu_0 \boldsymbol{\varepsilon}^- \cdot \boldsymbol{\varepsilon}^- \tag{31}$$

with $\boldsymbol{\varepsilon}^+ = \sum_i \langle \varepsilon_i \rangle_+ \boldsymbol{e}_i \otimes \boldsymbol{e}_i$ and $\boldsymbol{\varepsilon}^- = \sum_i \langle \varepsilon_i \rangle_- \boldsymbol{e}_i \otimes \boldsymbol{e}_i$, $\varepsilon_i$ being the eigenvalues of the strain tensor and $\boldsymbol{e}_i$ the corresponding eigenvectors. The residual stress tensor

$$\boldsymbol{\sigma}_R(\boldsymbol{\varepsilon}) = \lambda_0 \langle \mathrm{tr}(\boldsymbol{\varepsilon})\rangle_- \mathbf{I} + 2\mu_0 \boldsymbol{\varepsilon}^- \tag{32}$$

is non-zero also for $\mathrm{tr}(\boldsymbol{\varepsilon}) > 0$. Hence, residual stresses with negative trace are possible for strain tensors with positive trace. As we will show through a numerical example in Section 5, this undesirable coupling between tension and compression behavior is problematic during damage propagation.

The elastic domains $\mathcal{R}(\alpha)$ and $\mathcal{R}^*(\alpha)$ are detailed in Appendix A.2. The stress-based domain $\mathcal{R}^*(\alpha)$ does not evolve as a simple homothety centered in the origin with respect to $\alpha$, see Figure 3. We plot the elastic domains only in the space of the principal components, because the model cannot be expressed as a function of the volumetric and deviatoric parts of the strain/stress tensors. Since $\mathcal{R}^*(\alpha)$ is not a homotethy, we cannot define a unique damage value $\alpha_{\text{peak}}$ which marks the transition between stress-hardening and stress-softening behavior. With increasing damage, $\mathcal{R}^*(\alpha)$ shrinks only along tensile-dominated stress states. On the other hand, the compression-dominated strength does not necessarily have to decrease with increasing damage. Therefore, even though the evolution of $\mathcal{R}^*(\alpha)$ does not fulfill stress-softening for compression-dominated stress states, it still consistently represents damaging behavior. The asymmetry in tension and compression is gained at the expense of the existence of residual stresses. However, the compressive and shear strengths cannot be calibrated independently of the tensile strength even though they are different from those of the standard model (see Table 1).

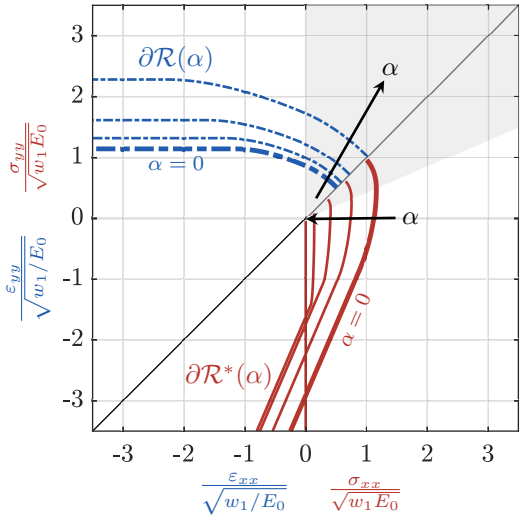


Fig. 3: Elastic domains for the model with spectral split in the strain (blue dash-dotted line) and stress (red solid line) space for $\alpha = \{0, 0.25, 0.5, 0.75, 1\}$ ($\nu_0 = 0.3$). The domains for $\alpha = 0$ are the nucleation domains (or strength surfaces). The grey background indicates the parts of the elastic domains shared with the standard model. Principal components diagram under the plane-strain assumption.

### *3.3. The no-tension model*

Freddi and Royer-Carfagni in [15] use the theory of structured deformations of Del Piero and Owen [39] to propose a new elastic energy decomposition. They also demonstrate that certain decompositions already available in literature [13, 40] and the standard model can be derived by leaning on this theory.

The assumption made is that the existence of micro-cracks leads to a reduction in the elastic energy density of the sound material $\varphi_0(\boldsymbol{\varepsilon})$ due to the presence of inelastic deformations known as *structured deformations*, denoted as $\boldsymbol{\eta}$. These structured deformations are constrained within a convex set $\mathcal{K}_\varepsilon$, which defines the admissible "structure" of the micro-cracks. With $\varphi_0(\boldsymbol{\varepsilon})$ and $\mathcal{K}_\varepsilon$ determined, the residual elastic energy is computed by solving the following minimization problem

$$\bar{\boldsymbol{\eta}}(\boldsymbol{\varepsilon}) := \arg\min_{\boldsymbol{\eta}\in\mathcal{K}_\varepsilon} \varphi_0(\boldsymbol{\varepsilon}-\boldsymbol{\eta}), \qquad \varphi_R(\boldsymbol{\varepsilon}) := \min_{\boldsymbol{\eta}\in\mathcal{K}_\varepsilon} \varphi_0(\boldsymbol{\varepsilon}-\boldsymbol{\eta}) = \varphi_0(\boldsymbol{\varepsilon}-\bar{\boldsymbol{\eta}}(\boldsymbol{\varepsilon})). \tag{33}$$

They apply the result of the minimization problem (33), reported in Appendix A.3, to the elastic energy density decomposition and then derive $\varphi_D(\boldsymbol{\varepsilon}) = \varphi_0(\boldsymbol{\varepsilon}) - \varphi_R(\boldsymbol{\varepsilon})$. By knowing $\varphi_D$ and $\varphi_R$, one can also derive the residual stresses as follows:

– if $\varepsilon_3 \geq 0$, $\boldsymbol{\sigma}_R = \mathbf{0}$,

– else if $\varepsilon_2 + \nu_0\varepsilon_3 \geq 0$, $\boldsymbol{\sigma}_R = \frac{\mu_0(3\lambda_0+2\mu_0)}{\lambda_0+\mu_0}\varepsilon_3 \boldsymbol{e}_3 \otimes \boldsymbol{e}_3$,

– else if $\varepsilon_1 + \frac{\nu_0}{1-\nu_0}(\varepsilon_2 + \varepsilon_3) \geq 0$, $\boldsymbol{\sigma}_R = \frac{2\mu_0}{\lambda_0+2\mu_0}\Big[ - \frac{\lambda_0(3\lambda_0+2\mu_0)(\varepsilon_2+\varepsilon_3)}{\lambda_0+2\mu_0}\boldsymbol{e}_1 \otimes \boldsymbol{e}_1 +$
$+ (2(\lambda_0 + \mu_0)\varepsilon_3 + \lambda_0\varepsilon_2)\,\boldsymbol{e}_2 \otimes \boldsymbol{e}_2 + (2(\lambda_0 + \mu_0)\varepsilon_2 + \lambda_0\varepsilon_3)\,\boldsymbol{e}_3 \otimes \boldsymbol{e}_3\Big]$,

– else, $\boldsymbol{\sigma}_R = 2\mu_0\boldsymbol{\varepsilon} + \lambda_0 \mathrm{tr}(\boldsymbol{\varepsilon})\mathbf{I}$.

The elastic domains are detailed in Appendix A.3 and represented in Figure 4 only in the space of principal components, because the model cannot be expressed as a function of the volumetric and deviatoric parts of the strain/stress tensors. With the no-tension model, the degree of asymmetry between tension and compression behavior is increased compared to the volumetric-deviatoric or the spectral splits. However, the model has some limitations common to the previous ones. The residual stresses lead to the same problematic coupling obtained with the spectral split. Furthermore, Chambolle et al. [38] study the behavior of this model as $\ell \to 0$ and demonstrate that a relative displacement of the crack faces results in infinite energy. This constraint does not physically describe a crack. In addition, there is still no flexibility in the choice of the compressive and shear strengths (see Table 1).

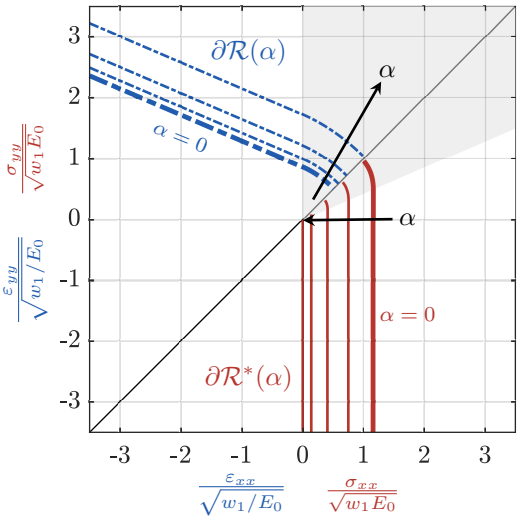


Fig. 4: Elastic domains for the no-tension model in the strain (blue dash-dotted line) and stress (red solid line) space for $\alpha = \{0, 0.25, 0.5, 0.75, 1\}$ ($\nu_0 = 0.3$). The domains for $\alpha = 0$ are the nucleation domains (or strength surfaces). The grey background indicates the parts of the elastic domains shared with the standard model. Principal components diagram under the plane-strain assumption.

### *3.4. The Drucker-Prager-like (DP-like) model*

The introduction of structured deformations potentially leads to extra flexibility, namely in the selection of the convex set $\mathcal{K}_\varepsilon$. De Lorenzis and Maurini [12] leverage this flexibility by introducing a new decomposition that depends on an additional material parameter $\gamma$. This parameter allows for elastic domains which partially recover the Drucker-Prager model, commonly used for modeling compressive failure in cohesive-frictional materials like rocks or concrete, and allow for an independent calibration of the tensile and the compressive or shear strengths.

The residual energy is determined through the structured deformation problem (33), utilizing a convex cone of admissible structured deformations

$$\mathcal{K}_\varepsilon := \{\boldsymbol{\eta} \in \mathrm{Sym} : \mathrm{tr}(\boldsymbol{\eta}) \geq \gamma|\boldsymbol{\eta}_{\mathrm{dev}}|\} \qquad \text{with } \gamma \geq 0. \tag{34}$$

The elastic strain energy decomposition, solution of the minimization problem (33), is detailed in Appendix A.4. The residual stresses read as follows:

| Decomposition | $\sigma_e^+$ | $\sigma_e^-$ | $\tau_e$ |
|---|---|---|---|
| None | $\sqrt{\frac{2E_0}{s'(0)}w_1 w'(0)}$ | $-\sqrt{\frac{2E_0}{s'(0)}w_1 w'(0)}$ | $\sqrt{\frac{2\mu_0}{s'(0)}w_1 w'(0)}$ |
| Vol.-dev. | $\sqrt{\frac{2E_0}{s'(0)}w_1 w'(0)}$ | $-\sqrt{\frac{6\mu_0}{s'(0)}w_1 w'(0)}$ | $\sqrt{\frac{2\mu_0}{s'(0)}w_1 w'(0)}$ |
| Spectral | $\sqrt{\frac{2E_0(1+\nu_0)}{1+\nu_0-2\nu_0^2}\frac{w_1 w'(0)}{s'(0)}}$ | $-\sqrt{\frac{E_0(1+\nu_0)}{\nu_0^2}\frac{w_1 w'(0)}{s'(0)}}$ | $\sqrt{\frac{4\mu_0}{s'(0)}w_1 w'(0)}$ |
| No-tension | $\sqrt{\frac{2E_0(1-\nu_0)}{1-\nu_0-2\nu_0^2}\frac{w_1 w'(0)}{s'(0)}}$ | $-\infty$ | $\sqrt{\frac{2E_0(1-\nu_0)}{1-\nu_0-2\nu_0^2}\frac{w_1 w'(0)}{s'(0)}}$ |
| DP-like | $\begin{cases}\sqrt{\frac{2E_0}{s'(0)}w_1 w'(0)} & \text{for } 0<\gamma<\sqrt{\frac{2}{3}}\frac{\mu_0}{\kappa_0}\\ \sqrt{\frac{18(\kappa_0\gamma^2+2\mu_0)}{(\sqrt{6}+\gamma)^2}\frac{w_1 w'(0)}{s'(0)}} & \text{for } \gamma\geq\sqrt{\frac{2}{3}}\frac{\mu_0}{\kappa_0}\end{cases}$ | $\begin{cases}-\sqrt{\frac{18(\kappa_0\gamma^2+2\mu_0)}{(\sqrt{6}-\gamma)^2}\frac{w_1 w'(0)}{s'(0)}} & \text{for } 0\leq\gamma<\sqrt{6}\\ -\infty & \text{for } \gamma\geq\sqrt{6}\end{cases}$ | $\sqrt{(\kappa_0\gamma^2+2\mu_0)\frac{w_1 w'(0)}{s'(0)}}$ |
| Star-convex | $\sqrt{\frac{2E_0}{s'(0)}w_1 w'(0)}$ | $\begin{cases}-\sqrt{\frac{2E_0}{1+(1+\gamma^\star)\frac{(n-1)\nu_0-1}{n}}\frac{w_1 w'(0)}{s'(0)}} & \text{for } -1\leq\gamma^\star<\frac{n(n-1)}{2}\frac{\kappa_0}{\mu_0}\\ -\infty & \text{for } \gamma^\star\geq\frac{n(n-1)}{2}\frac{\kappa_0}{\mu_0}\end{cases}$ | $\sqrt{\frac{2\mu_0}{s'(0)}w_1 w'(0)}$ |

Tab. 1: Tensile, compressive and shear strengths for all the analyzed models.

– if $|\boldsymbol{\varepsilon}_{\text{dev}}| < \text{tr}(\boldsymbol{\varepsilon})/\gamma$, $\boldsymbol{\sigma}_R = \mathbf{0}$,

– else if $|\boldsymbol{\varepsilon}_{\text{dev}}| \geq -\frac{\gamma\kappa_0}{2\mu_0}\text{tr}(\boldsymbol{\varepsilon})$, $\boldsymbol{\sigma}_R = \frac{2\kappa_0\mu_0}{\kappa_0\gamma^2+2\mu_0}\left((\text{tr}\boldsymbol{\varepsilon} - \gamma|\boldsymbol{\varepsilon}_{\text{dev}}|)\mathbf{I} + \gamma\left(\gamma - \frac{\text{tr}\boldsymbol{\varepsilon}}{|\boldsymbol{\varepsilon}_{\text{dev}}|}\right)\boldsymbol{\varepsilon}_{\text{dev}}\right)$,

– else, $\boldsymbol{\sigma}_R = 2\mu_0\boldsymbol{\varepsilon}_{\text{dev}} + \kappa_0\text{tr}(\boldsymbol{\varepsilon})\mathbf{I}$.

With this model, the shear or the compressive strength can be calibrated independently of the tensile strength through the new parameter $\gamma$ (see Figure 5 and 6). However, during damage evolution the residual stresses lead to the same undesired coupling between tension and compression as with the spectral split and the no-tension model.

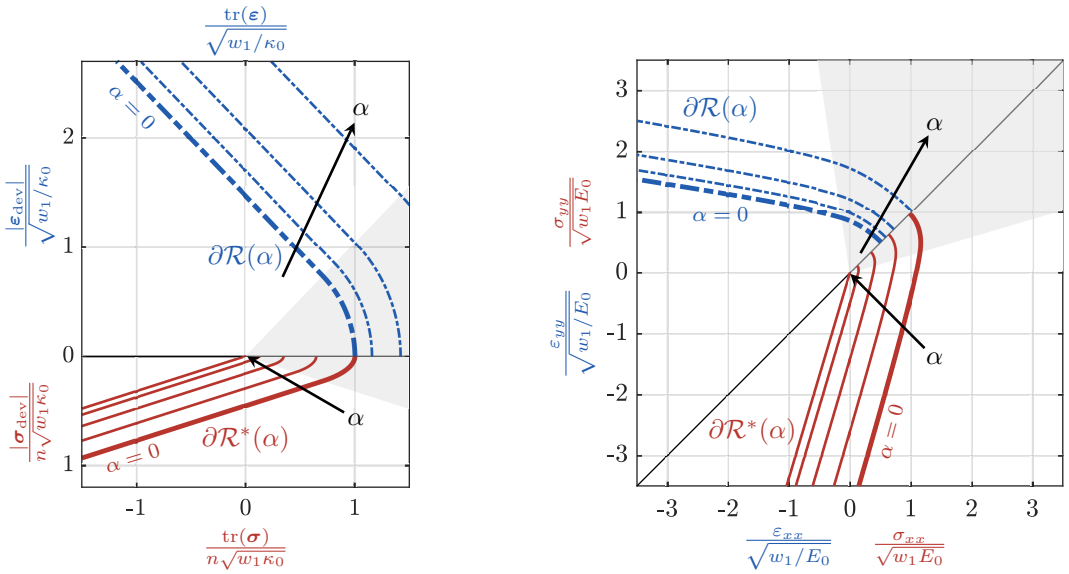


(a) (b)

Fig. 5: Elastic domains for the DP-like model in the strain (blue dash-dotted line) and stress (red solid line) space for $\alpha = \{0, 0.25, 0.5, 0.75, 1\}$ and $\gamma = \sqrt{2\mu_0/\kappa_0}$ ($\nu_0 = 0.3$). The domains for $\alpha = 0$ are the nucleation domains (or strength surfaces). The grey background indicates the parts of the elastic domains shared with the standard model. Volumetric-deviatoric diagram (a). Principal components diagram under the plane-strain assumption (b).

### *3.5. Summary*

In light of the requirements defined in Section 2.4, we summarize the merits and disadvantages of the analyzed models in Table 2. None of the available splits meets all requirements, as they either lack in flexibility (a requisite that

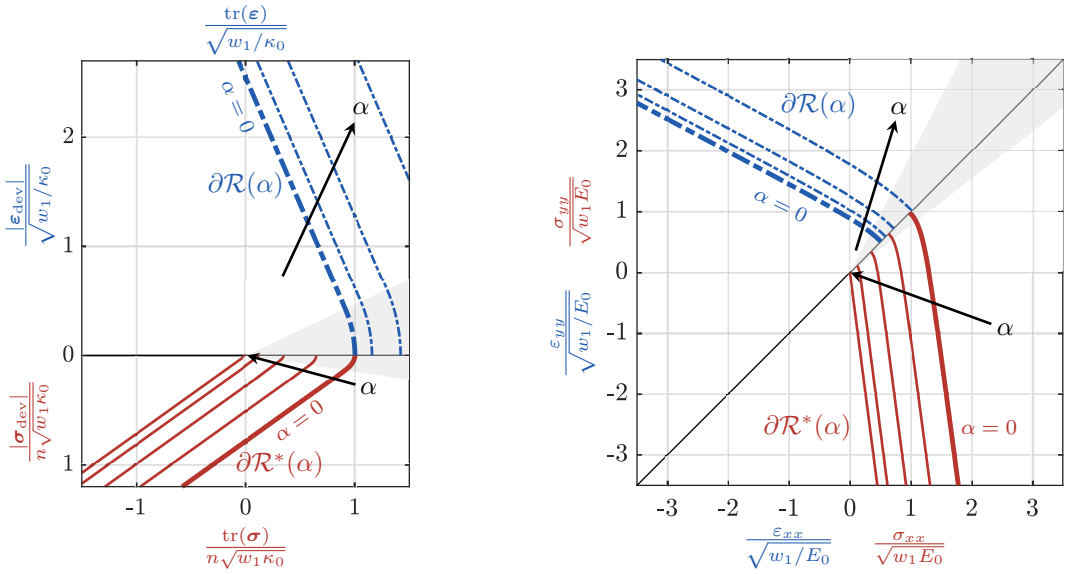


(a) (b)

Fig. 6: Elastic domains for the DP-like model in the strain (blue dash-dotted line) and stress (red solid line) space for $\alpha = \{0, 0.25, 0.5, 0.75, 1\}$ and $\gamma = \sqrt{10\mu_0/\kappa_0}$ ($\nu_0 = 0.3$). The domains for $\alpha = 0$ are the nucleation domains (or strength surfaces). The grey background indicates the parts of the elastic domains shared with the standard model. Volumetric-deviatoric diagram (a). Principal components diagram under the plane-strain assumption (b).

is most important for nucleation, since this defines the strength surface of the material) or give rise to residual stresses which contain spurious components (a requisite that is most important for damage evolution and for obtaining a crack-like behavior of the fully developed damage localization bands). With the goal of satisfying the above requirements under both aspects of flexibility and crack-like residual stresses, in the next section we introduce a novel model, which we denote as the star-convex model.

| | Strain-hardening | Stress-softening | Tens./compr. asymmetry | Flexibility | Crack-like residual stress |
|---|---|---|---|---|---|
| Standard | ✓ | ✓ | ✗ | ✗ | ✗ |
| Vol.-dev. | ✓ | ✓ | ✓ | ✗ | ✓ |
| Spectral | ✓ | ✗ | ✓ | ✗ | ✗ |
| No-tension | ✓ | ✓ | ✓ | ✗ | ✗ |
| DP-like | ✓ | ✓ | ✓ | ✓* | ✗ |
| Star-convex | ✓ | ✓ | ✓ | ✓** | ✓ |

*: Partial flexibility: out of tensile, compressive and shear strengths, the model allows for independent calibration of any pair, while the third property is automatically fixed. **: Partial flexibility: the model allows for independent calibration of tensile and compressive or shear and compressive strengths, while the third property is automatically fixed.

Tab. 2: Analyzed models and requirements to an ideal model for multi-axial stress states: blue checks and red crosses denote respectively success and failure in satisfying a requirement. The star-convex meets all requirements with partial flexibility.

## 4. The star-convex model

In this section, we propose a new model that aims at satisfying the model requirements defined in Section 2.4. As mentioned earlier, in [38] it is shown that the volumetric-deviatoric split can be used to approximate the non-interpenetration constraint in the sense of Γ-convergence. This success hinges on a residual elastic strain energy density depending solely on the volumetric energy associated to a negative trace, i.e. $\varphi_R(\boldsymbol{\varepsilon}) \propto \langle \mathrm{tr}(\boldsymbol{\varepsilon})\rangle_-^2$. All the

other decompositions suffer from spurious non-zero tangential stiffness for fully developed cracks. Therefore, the volumetric-deviatoric split represents a sound option to model crack-like stresses in the phase-field framework, but lacks flexibility in calibrating the compressive strength $\sigma_e^-$ independently of the tensile strength $\sigma_e^+$. To compensate for this disadvantage but keep a residual part exclusively related to a local volume contraction $\langle \mathrm{tr}(\boldsymbol{\varepsilon})\rangle_-$, we propose the following energy decomposition

$$\begin{aligned}\varphi_D(\boldsymbol{\varepsilon}) =& \mu_0 \left|\boldsymbol{\varepsilon}_{\mathrm{dev}}\right|^2 + \frac{1}{2}\,\kappa_0 \left(\langle \mathrm{tr}(\boldsymbol{\varepsilon})\rangle_+^2 - \gamma^\star \langle \mathrm{tr}(\boldsymbol{\varepsilon})\rangle_-^2\right),\\ \varphi_R(\boldsymbol{\varepsilon}) =& (1+\gamma^\star)\,\frac{1}{2}\,\kappa_0 \langle \mathrm{tr}(\boldsymbol{\varepsilon})\rangle_-^2,\end{aligned} \tag{35}$$

where $\gamma^\star \geq -1$ is the additional parameter controlling the $\sigma_e^-/\sigma_e^+$ ratio. Hence, the volumetric and deviatoric components of the stress are derived as

$$\begin{aligned}\boldsymbol{\sigma}_{\mathrm{vol}} =& \kappa_0 \left\{a(\alpha)\langle \mathrm{tr}(\boldsymbol{\varepsilon})\rangle_+ + \left[1+\gamma^\star\,(1-a(\alpha))\right]\langle \mathrm{tr}(\boldsymbol{\varepsilon})\rangle_-\right\}\mathbf{I},\\ \boldsymbol{\sigma}_{\mathrm{dev}} =& 2a(\alpha)\mu_0 \boldsymbol{\varepsilon}_{\mathrm{dev}}.\end{aligned} \tag{36}$$

For a reason that will become clear later, we denote the corresponding model as *star-convex model* (or star-convex energy decomposition). In the following subsections, we analyze the elastic domains for the proposed model in the strain and stress spaces. In Appendix B, we provide further insights on the development of the proposed model in comparison to alternative options.

### *4.1. Strain space*

Figures 7-9 illustrate the elastic domain of the proposed model in the strain space, which is given by the conditions

$$\begin{cases}\mu_0 \left|\boldsymbol{\varepsilon}_{\mathrm{dev}}\right|^2 + \frac{\kappa_0}{2}\,\mathrm{tr}(\boldsymbol{\varepsilon})^2 \leq -\frac{w_1 w'(\alpha)}{a'(\alpha)} & \text{for} \quad \mathrm{tr}(\boldsymbol{\varepsilon}) \geq 0\\ \mu_0 \left|\boldsymbol{\varepsilon}_{\mathrm{dev}}\right|^2 - \gamma^\star \frac{\kappa_0}{2}\,\mathrm{tr}(\boldsymbol{\varepsilon})^2 \leq -\frac{w_1 w'(\alpha)}{a'(\alpha)}, & \text{for} \quad \mathrm{tr}(\boldsymbol{\varepsilon}) < 0\end{cases}.$$

For $\mathrm{tr}(\boldsymbol{\varepsilon}) \geq 0$, the new model shares the same boundary of the elastic domain $\partial\mathcal{R}(\alpha)$ with the standard model and $\partial\mathcal{R}(\alpha)$ is an ellipse in the $\mathrm{tr}(\boldsymbol{\varepsilon}) - |\boldsymbol{\varepsilon}_{\mathrm{dev}}|$ diagram. On the same diagram but for $\mathrm{tr}(\boldsymbol{\varepsilon}) < 0$, the parameter $\gamma^\star$ determines the type of conic section (Figure 7) such that

- for $-1 \leq \gamma^\star < 0$, $\partial\mathcal{R}(\alpha)$ is an ellipse,
- for $\gamma^\star = 0$, $\partial\mathcal{R}(\alpha)$ is a degenerate parabola (horizontal straight line),
- for $\gamma^\star > 0$, $\partial\mathcal{R}(\alpha)$ is a hyperbola lying above the asymptote $|\boldsymbol{\varepsilon}_{\mathrm{dev}}| = -\sqrt{\frac{\kappa_0}{2\mu_0}\,\gamma^\star}\,\mathrm{tr}(\boldsymbol{\varepsilon})$

In particular, we retrieve the standard model when $\gamma^\star = -1$ and the volumetric-deviatoric split for $\gamma^\star = 0$.

For $-1 \leq \gamma^\star \leq 0$, the elastic domain $\mathcal{R}(\alpha)$ is convex, whereas for $\gamma^\star > 0$ $\partial\mathcal{R}(\alpha)$ consists of the ellipse defined over $\mathrm{tr}(\boldsymbol{\varepsilon}) > 0$ smoothly joined at $\mathrm{tr}(\boldsymbol{\varepsilon}) = 0$ with the hyperbola defined over $\mathrm{tr}(\boldsymbol{\varepsilon}) < 0$. Hence, in this case $\mathcal{R}(\alpha)$ is not convex but rather $\mathbf{0}$-star-convex, i.e. $\forall \boldsymbol{\varepsilon} \in \mathcal{R}(\alpha)$ and $\forall s \in [0,1]$, $s\boldsymbol{\varepsilon} \in \mathcal{R}(\alpha)$ [41]. This is the reason for denoting the new model as *star-convex model* (or star-convex decomposition). In [33] it is shown that an elastic-plastic material with non-negative interior work in an admissible strain cycle must have a convex elastic domain. However, the same thermodynamic work property assumed for an elastic-damaging material does not necessarily imply convexity, but at most star-convexity with respect to $\mathbf{0}$.

The star-convex model enjoys the strain-hardening property $\forall \alpha \in [0,1)$. Additionally, for $\gamma^\star > 0$, the hyperbola for $\mathrm{tr}(\boldsymbol{\varepsilon}) < 0$ evolves but keeps a constant asymptote as this depends only on the elastic constants and on $\gamma^\star$. Since $\partial\mathcal{R}(\alpha)$ lies above the asymptote (grey dashed line in Figure 7), the strain states below the asymptote are unable to produce additional damage and the material behaves as linearly elastic. Accordingly, the compressive strength can be calibrated by modifying the slope of the asymptote by tuning $\gamma^\star$, thus providing the desired flexibility in nucleation. At the limit $\alpha = 1$, the star-convex elastic domain becomes $\mathcal{R}(1) = \mathrm{Sym}$, meaning that for a fully broken material the whole strain space is admissible.

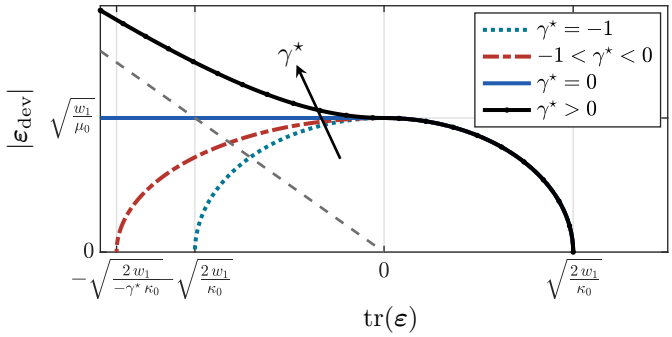


Fig. 7: Nucleation domain in the strain space for the star-convex model with varying $\gamma^\star$ ($\nu_0 = 0.3$). For $\mathrm{tr}(\boldsymbol{\varepsilon}) < 0$, the boundary is an ellipse if $-1 \leq \gamma^\star < 0$, a degenerate parabola if $\gamma^\star = 0$ and a hyperbola (with the dashed grey line as asymptote) if $\gamma^\star > 0$.

### *4.2. Stress space*

The elastic domain in the stress space $\mathcal{R}^*(\alpha)$ (Figures 8, 9) is the set of $\boldsymbol{\sigma} \in \mathrm{Sym}$ such that

– if $\mathrm{tr}(\boldsymbol{\sigma}) \geq 0$, $\frac{1}{4\,\mu_0}\,|\boldsymbol{\sigma}_{\mathrm{dev}}|^2 + \frac{1}{2\,\kappa_0\,n^2}\,\mathrm{tr}(\boldsymbol{\sigma})^2 \leq \frac{w_1 w'(\alpha)}{s'(\alpha)}$,

– if $\mathrm{tr}(\boldsymbol{\sigma}) < 0$, $\frac{1}{4\,\mu_0}\,|\boldsymbol{\sigma}_{\mathrm{dev}}|^2 - \gamma^\star\,\frac{a(\alpha)^2}{2\,\kappa_0\,n^2\,(1+\gamma^\star\,(1-a(\alpha)))^2}\,\mathrm{tr}(\boldsymbol{\sigma})^2 \leq \frac{w_1 w'(\alpha)}{s'(\alpha)}$.

Similarly to the strain space, for $\mathrm{tr}(\boldsymbol{\sigma}) \geq 0$ the star-convex split shares with the standard model the same elliptic boundary $\partial\mathcal{R}^*(\alpha)$ in the $\mathrm{tr}(\boldsymbol{\sigma}) - |\boldsymbol{\sigma}_{\mathrm{dev}}|$ diagram, whereas for $\mathrm{tr}(\boldsymbol{\sigma}) < 0$

- for $-1 \leq \gamma^\star < 0$, $\partial\mathcal{R}^*(\alpha)$ is an ellipse,
- for $\gamma^\star = 0$, $\partial\mathcal{R}^*(\alpha)$ is a degenerate parabola (horizontal straight line),
- for $\gamma^\star > 0$, $\partial\mathcal{R}^*(\alpha)$ is a hyperbola lying above the asymptote $|\boldsymbol{\sigma}_{\mathrm{dev}}| = -\frac{2\,a(\alpha)}{n(1+\gamma^\star(1-a(\alpha)))}\,\sqrt{\frac{2\mu_0}{\kappa_0}\,\gamma^\star}\,\mathrm{tr}(\boldsymbol{\sigma})$.

A three-dimensional representation of $\mathcal{R}^*(0)$ is given for $\gamma^\star = 1, 5$ in Figure 10. For $-1 \leq \gamma^\star \leq 0$, the domain $\mathcal{R}^*(\alpha)$ is convex, whereas for $\gamma^\star > 0$ $\mathcal{R}^*(\alpha)$ is not convex but $\mathbf{0}-$star-convex, i.e. $\forall \boldsymbol{\sigma} \in \mathcal{R}^*(\alpha)$ and $\forall s \in [0, 1]$, $s\boldsymbol{\sigma} \in \mathcal{R}^*(\alpha)$ [41].

The star-convex model enjoys the stress-softening property $\forall \alpha \in [0, 1)$. At the limit $\alpha = 1$, the star-convex elastic domain becomes strictly convex and collapses to the negative hydrostatic pressure half-line, meaning that non-zero deviatoric and positive volumetric stresses are not admissible in a fully broken material. In particular, according to (24), the stress tensor when $\alpha = 1$ is

$$\boldsymbol{\sigma}_R = (1 + \gamma^\star)\,\kappa_0\,\langle \mathrm{tr}(\boldsymbol{\varepsilon})\rangle_-\,\boldsymbol{I}, \tag{37}$$

thus, the mapping between admissible strains and admissible stresses for $\alpha = 1$ is such that only negative volumetric strains can produce work through negative volumetric stresses. In this manner, the model fulfils the crack-like stress requirement.

Equation (37) shows that, for negative volumetric strains, the volumetric stiffness for $\alpha = 1$ is $\kappa_0(1 + \gamma^\star)$. On the other hand, according to (36), it is equal to $\kappa_0$ when $\alpha = 0$. Therefore, for negative volumetric strains, the volumetric stiffness of a fully broken material is larger than the one of the pristine material when $\gamma^\star > 0$. This increase can be explained by considering that the damage evolution occurs only above the asymptote, where the deviatoric contribution exceeds the volumetric one. Damage evolution redistributes the stiffness such that the deviatoric stiffness decreases to zero and the volumetric stiffness increases, while the total elastic energy density (which is the sum of the volumetric and deviatoric contributions) always decreases.

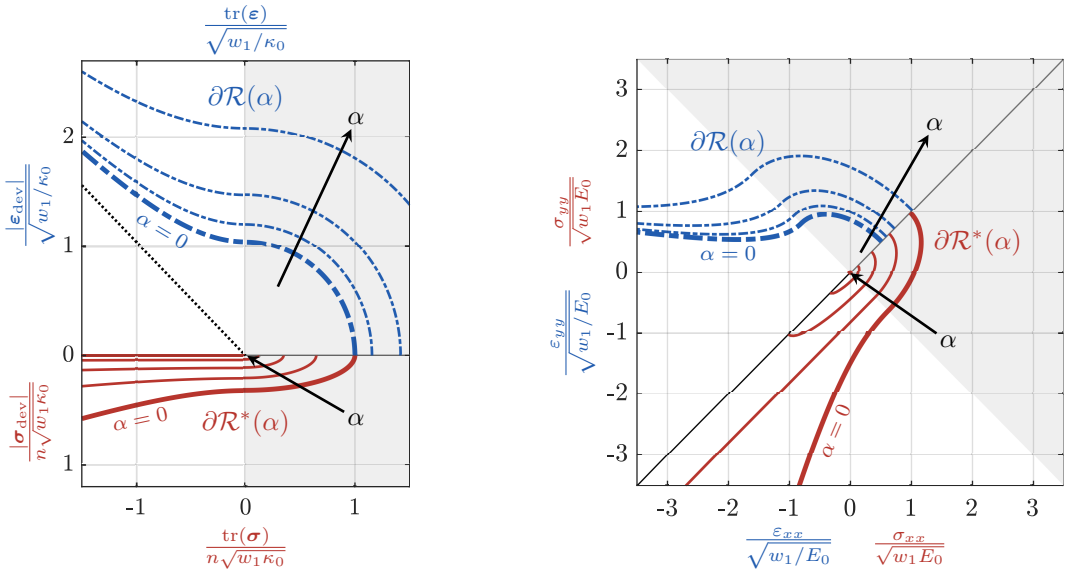


(a) (b)

Fig. 8: Elastic domains for the star-convex model in the strain (blue dash-dotted line) and stress (red solid line) space for $\alpha = \{0, 0.25, 0.5, 0.75, 1\}$ for $\gamma^\star = 1$ ($\nu_0 = 0.3$). The domains for $\alpha = 0$ are the nucleation domains (or strength surfaces). The grey background indicates the parts of the elastic domains shared with the standard model. Volumetric-deviatoric diagram (a): damage cannot evolve for loading directions below the black dashed line in the strain space which is also the constant asymptote. Principal components diagram under the plane-strain assumption (b).

Defining as usual the strength surface as the boundary of the elastic domain in the stress space for $\alpha = \alpha_{peak} = 0$, i.e. $\partial\mathcal{R}^*(0)$, we can derive the tensile strength, the shear strength and the compressive strength as

$$\sigma_e^+ = \sqrt{\frac{2\,E_0\,w_1\,w'(0)}{s'(0)}}, \quad \tau_e = \sqrt{\frac{2\,\mu_0\,w_1\,w'(0)}{s'(0)}},$$
$$\sigma_e^- = \begin{cases} -\sqrt{\frac{1}{1+(1+\gamma^\star)\,\frac{(n-1)\,\nu-1}{n}}\,\frac{2\,E_0\,w_1\,w'(0)}{s'(0)}} & \text{for} \quad \gamma^\star < \frac{n(n-1)}{2}\,\frac{\kappa_0}{\mu_0}, \\ -\infty & \text{otherwise.} \end{cases} \tag{38}$$

From (38) we see that the shear strength $\tau_e$ is independent of $\gamma^\star$. Thus, the flexibility offered by the star-convex model is exclusively related to the compressive stength $\sigma_e^-$.

## 5. Numerical tests

As follows, we demonstrate the advantages and limitations of the existing models outlined in Section 3 and of the novel star-convex model introduced in Section 4 through numerical experiments. These consist in a bi-axially loaded disk, a plate with hole under compression and two blocks in relative sliding.

Computational solvers for phase-field fracture models based on the finite element method seek a quasi-static solution by solving the time- and space-discretized weak problem. At time step $t$, we look for the solution of the space-discretized weak form of (8) and (9) by using an alternate minimization scheme implemented in FEniCSx [42, 43]. In [6], such scheme was introduced in the context of the standard model taking advantage of the separate directional convexity of functions $\boldsymbol{u} \to \mathcal{E}_t(\boldsymbol{u}, \cdot)$ and $\alpha \to \mathcal{E}_t(\cdot, \alpha)$ (see also [44, 45] for a detailed discussion on monolithic and alternate minimization schemes). With this scheme, using as initial guess $(\boldsymbol{u}^{k-1}, \alpha^{k-1})$, we first solve the problem in $\boldsymbol{u}$ using a Newton-based nonlinear solver with line search and a maximum of 100 iterations, which gives us the output $\boldsymbol{u}^k$. Then, starting from $(\boldsymbol{u}^k, \alpha^{k-1})$, we solve the constrained nonlinear problem in $\alpha$ using a reduced-space

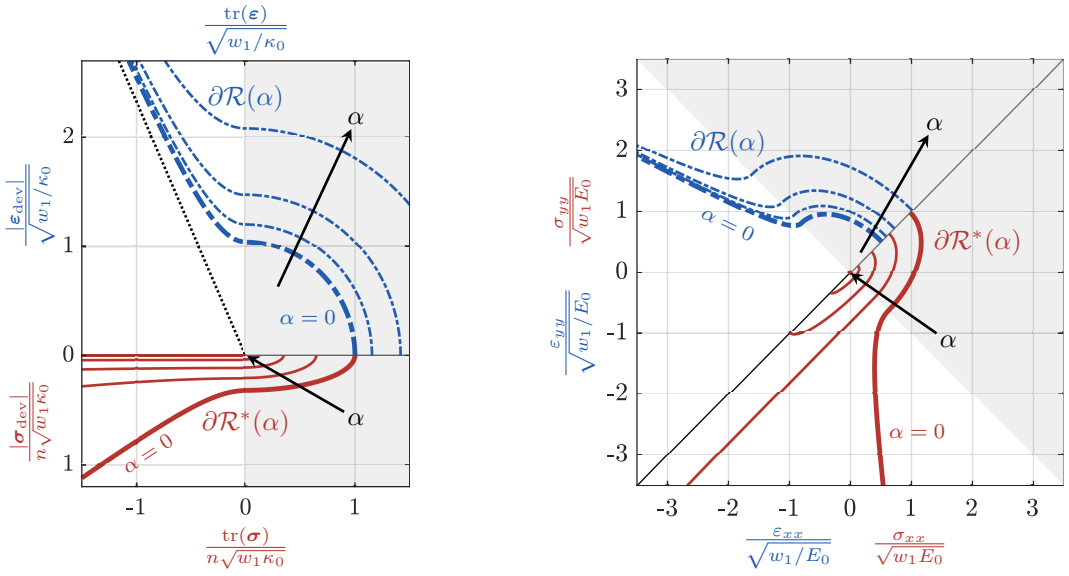


Fig. 9: Elastic domains for the star-convex model in the strain (blue dash-dotted line) and stress (red solid line) space for $\alpha = \{0, 0.25, 0.5, 0.75, 1\}$ and $\gamma^\star = 5$ ($\nu_0 = 0.3$). The domains for $\alpha = 0$ are the nucleation domains (or strength surfaces). The grey background indicates the parts of the elastic domains shared with the standard model. Volumetric-deviatoric diagram (a): damage cannot evolve for loading directions below the black dashed line in the strain space which is also the constant asymptote. Principal components diagram under the plane-strain assumption (b).

active set solver for variational inequalities based on Newton's method with a maximum of 100 iterations, which returns $\alpha^k$. Consequently, we calculate $R_u$, the $L_2$-norm of the residual for the displacement problem for $(\boldsymbol{u}^k, \alpha^k)$. The convergence of the alternate minimization scheme is achieved if $R_u$ is below the tolerance level ($\texttt{tol} = 10^{-6}$) .

For $\mathrm{tr}(\boldsymbol{\varepsilon}) < 0$, the DP-like model and the star-convex model display a linearly elastic behavior with no damage for $|\boldsymbol{\varepsilon}_{\mathrm{dev}}| < -\frac{\gamma\kappa_0}{2\mu_0}\,\mathrm{tr}(\boldsymbol{\varepsilon})$ and $|\boldsymbol{\varepsilon}_{\mathrm{dev}}| < -\sqrt{\frac{\kappa_0}{2\mu_0}\,\gamma^\star}\,\mathrm{tr}(\boldsymbol{\varepsilon})$, respectively. By overlapping these two lines, we obtain the relationship $\gamma = \sqrt{2\gamma^\star\mu_0/\kappa_0}$ among the parameters $\gamma$ and $\gamma^\star$. Accordingly, we adopt $\gamma^\star = \{1, 5\}$ for the star-convex model and $\gamma = \{\sqrt{2\mu_0/\kappa_0}, \sqrt{10\mu_0/\kappa_0}\}$ for the DP-like model to facilitate their comparison.

### *5.1. Bi-axially loaded disk test*

We first focus on nucleation and consider a bi-axially loaded disk of diameter $D$ under the plane-strain assumption. The geometry and boundary conditions are illustrated in Figure 11. The center of the disk coincides with the origin of the cartesian reference system $x$-$y$ and the out-of-plane direction is denoted with $z$. We set $D = 1$, $E_0 = 100$, $\nu_0 = 0.3$, $w_1 = 1.5$ and $\ell = 0.04$. At $t = 0$, the material is assumed to be intact, i.e. $\alpha = 0$ everywhere. The goal of the test is to numerically determine the elastic domains of the various models for $\alpha = 0$ in the $\varepsilon_{xx}$-$\varepsilon_{yy}$ and $\sigma_{xx}$-$\sigma_{yy}$ planes.

Defining on the $\varepsilon_{xx}$-$\varepsilon_{yy}$ plane the angle $\theta \in [0, 2\pi)$, for a given $\theta$ we prescribe a displacement $\bar{\boldsymbol{u}}_t = t(x\cos(\theta), y\sin(\theta))$ on the disk boundary. In the linearly elastic regime, this Dirichlet boundary condition ensures that the disk is subjected to a homogeneous strain along the $\theta$-direction, i.e.

$$\frac{\varepsilon_{yy}}{\varepsilon_{xx}} = \tan(\theta). \tag{39}$$

Maintaining $\theta$ fixed, we increment the value of $t$ until we reach the elastic limit, while always imposing the Dirichlet boundary condition $\alpha = 0$ on the whole boundary of the disk. We discretize the problem with standard linear triangular finite elements using an unstructured mesh with average size $h = \ell/3$.

Figures 12 and 13 illustrate the contour of the elastic domain in the strain and stress planes at $\alpha = 0$ for all models. The blue and red lines correspond to the theoretical strain and stress domains, respectively, while the dots of the respective colors represent the numerically obtained strain and stress states right before damage nucleation. In

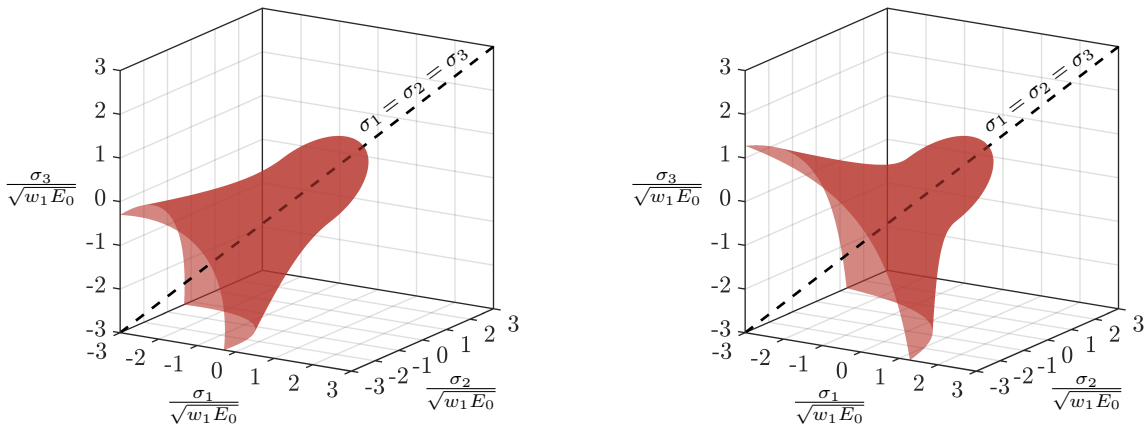


(a) $\gamma^\star = 1$ (b) $\gamma^\star = 5$

Fig. 10: Three-dimensional nucleation domain in the stress space for the star-convex model with $\gamma^\star = 1$ (a) and $\gamma^\star = 5$ (b) ($\nu_0 = 0.3$).

some cases, the dots are absent because certain loading directions do not reach the limit or reach it after a very large number of time steps (outside the range of the figure). For each load direction we plot the damage field at the time step when nucleation occurs, if it occurs; for directions at which no nucleation occurs we plot a zero damage field for completeness. Hence, the test serves not only as a nucleation test but also provides valuable insights into the initial crack propagation behavior under various loading conditions.

Figure 12a presents the simulation results for the standard model, which displays elliptical elastic domains and maintains symmetry of behavior in both tension and compression. Accordingly, the elastic domains are symmetric not only with respect to the bisector of the first and third quadrants but also with respect to the bisector of the second and fourth quadrants.

Figure 12b illustrates the outcomes of the test using the volumetric-deviatoric model. The "tensile" part ($\mathrm{tr}(\boldsymbol{\varepsilon}) \geq 0$)) behaves as in the standard model, while an asymmetry in the compressive behavior is introduced by the split. Due to the plane-strain assumption, there is no purely volumetric direction; as a result, the elastic domain is closed, leading to damage nucleation for every loading direction. In the third quadrant of Figure 12b nucleation occurs in all cases, although in three of them the damage level is so low to be hardly visible. Understanding why these cases nucleate but do not localize into a crack would require a second-order stability analysis for multi-axial stress states [8, 36], a task going beyond the scope of the present work and currently in progress [37].

Figures 12c and 12d provide the results for the spectral and the no-tension models, respectively. In these cases, the domains are open since for some directions (some values of $\theta$) nucleation cannot occur. The extent of the no-nucleation region varies for the spectral and the no-tension models but cannot be adjusted based on experimental results. As discussed in Section 3.2, the evolution of the elastic domain in the stress plane for the spectral split is a complex non-homothetic transformation with respect to the origin that does not enjoy the stress-softening property. This can explain the presence in Figure 12c of some localized damage fields not reaching $\alpha = 1$.

Figures 12e and 12f depict the results of the test using the DP-like model with $\gamma = \sqrt{2\mu_0/\kappa_0}$ and $\gamma = \sqrt{10\mu_0/\kappa_0}$, respectively. Similar to the spectral and no-tension models, the domains remain open, hence for some values of $\theta$ no nucleation occurs. However, the opening angle of the no-nucleation region can now be adjusted using the additional parameter $\gamma$, namely, it becomes wider with increasing $\gamma$. At the same time the region of $\partial\mathcal{R}(\alpha)$ and $\partial\mathcal{R}^*(\alpha)$ shared with the standard model becomes narrower as $\gamma$ increases. While on this shared region the nucleation behavior is the same as in the standard model (the dots have the same locations), the propagation behavior (which can be appreciated looking at the plotted localized damage fields after nucleation) is different. For instance, for $\gamma = \sqrt{10\mu_0/\kappa_0}$ in Figure 12f, the cracks exhibit abnormal thickening with respect to those in 12a even in the first quadrant where the shared portion lies. Hence, while this model exhibits the desired flexibility in nucleation, it leads to a problematic behavior during propagation related to the non-zero residual stresses for $\mathrm{tr}(\boldsymbol{\varepsilon}) > 0$.

Finally, Figures 13a and 13b illustrate the results for the star-convex split with $\gamma^\star = \{1, 5\}$. Similar to the DP-like

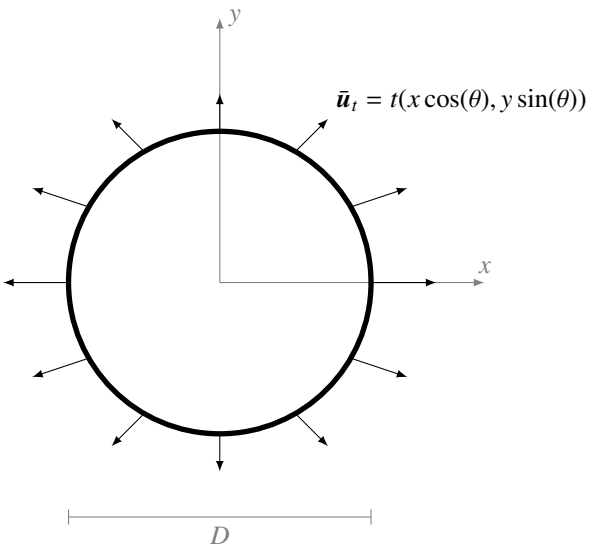


Fig. 11: Geometry and loading for the bi-axially loaded disk.

model, the star-convex split also exhibits a certain flexibility in the opening angle of the no-nucleation region. As shown in the figures, for increasing values of $\gamma^\star$, the opening angle widens. At the same time, the star-convex split shows a better propagation behavior without the abnormal thickening of cracks observed with the DP-like model. In fact, the residual stresses are entirely absent for $\mathrm{tr}(\boldsymbol{\varepsilon}) \geq 0$ and proportional to the volumetric strain in compression ($\mathrm{tr}(\boldsymbol{\varepsilon}) \leq 0$).

### *5.2. Plate with hole test*

We now discuss the compression of a plate with hole under plane-strain conditions. Assuming the problem to be symmetric, the test is performed on a quarter of the plate as shown in Figure 14.

The plate is a square with side length $2L$ and a central hole with radius $R$. The hole center coincides with the origin of both the cartesian reference system $x$-$y$ and the polar one $r$-$\theta$. The out-of-plane direction is denoted with $z$. Rigid body motions are prevented by the symmetry constraints $u_y(x, y = 0) = 0$ and $u_x(x = 0, y) = 0$ and compression is prescribed through the upper vertical displacement $u_y(x, y = L) = -tL$ with $t$ going from 0 up to 0.3. At $t = 0$, the material is assumed to be intact, i. e. $\alpha = 0$ everywhere. We adopt $L = 1$, $R = 0.3$, $E_0 = 100$, $\nu_0 = 0.3$, $w_1 = 1$ and $\ell = 0.02$. We discretize the problem with standard bilinear quadrilateral finite elements using an unstructured mesh with average size $h = \ell/3$.

During the elastic regime, the highest stress concentration is expected at the boundary of the hole ($r = R$), along which the radial stress $\sigma_{rr}$ and the tangential stress $\sigma_{r\theta}$ are both zero ($\sigma_{rr} = \sigma_{r\theta} = 0$) and the hoop stress $\sigma_{\theta\theta}$ and the out-of-plane stress $\sigma_{zz}$ are related by the plane-strain condition $\sigma_{zz} = -\nu_0\sigma_{\theta\theta}$. Along the boundary of the hole, point A ($r = R, \theta = \pi/2$) undergoes the maximum tensile hoop stress $\sigma^{\mathrm{A}}_{\theta\theta} \geq 0$ whereas point B ($r = R, \theta = 0$) is subjected to the lowest compressive hoop stress $\sigma^{\mathrm{B}}_{\theta\theta} \leq -\sigma^{\mathrm{A}}_{\theta\theta}$.

We now wonder whether the crack will originate from A or B. Experiments with this setup for many brittle materials produce a so-called "splitting" crack that starts at point A and proceeds parallel to the loading direction upwards [46]. On the other hand, nucleation as predicted by a phase-field model will start from the point at which the stress state first touches the limit curve $\partial\mathcal{R}^*(0)$. For first nucleation in A, the stress state in A must reach the intersection between $\partial\mathcal{R}^*(0)$ and the half-line $\sigma_{zz} = -\nu_0\sigma_{\theta\theta} \leq 0$. We denote with $\sigma^+_{\theta\theta_e}$ the value of the hoop stress at this intersection point (this concept is exemplified in Figure 15 for the star-convex model). Similarly, for first nucleation in B, the stress state in B must reach the intersection between $\partial\mathcal{R}^*(0)$ and the half-line $\sigma_{zz} = -\nu_0\sigma_{\theta\theta} \geq 0$. We denote with $\sigma^-_{\theta\theta_e}$ the value of the hoop stress at this intersection point (Figure 15). The $|\sigma^-_{\theta\theta_e}/\sigma^+_{\theta\theta_e}|$ ratio increases with the compressive to tensile strength ratio $|\sigma^-_e/\sigma^+_e|$ with a trend which is specific to each model. Since when $L \gg R$,

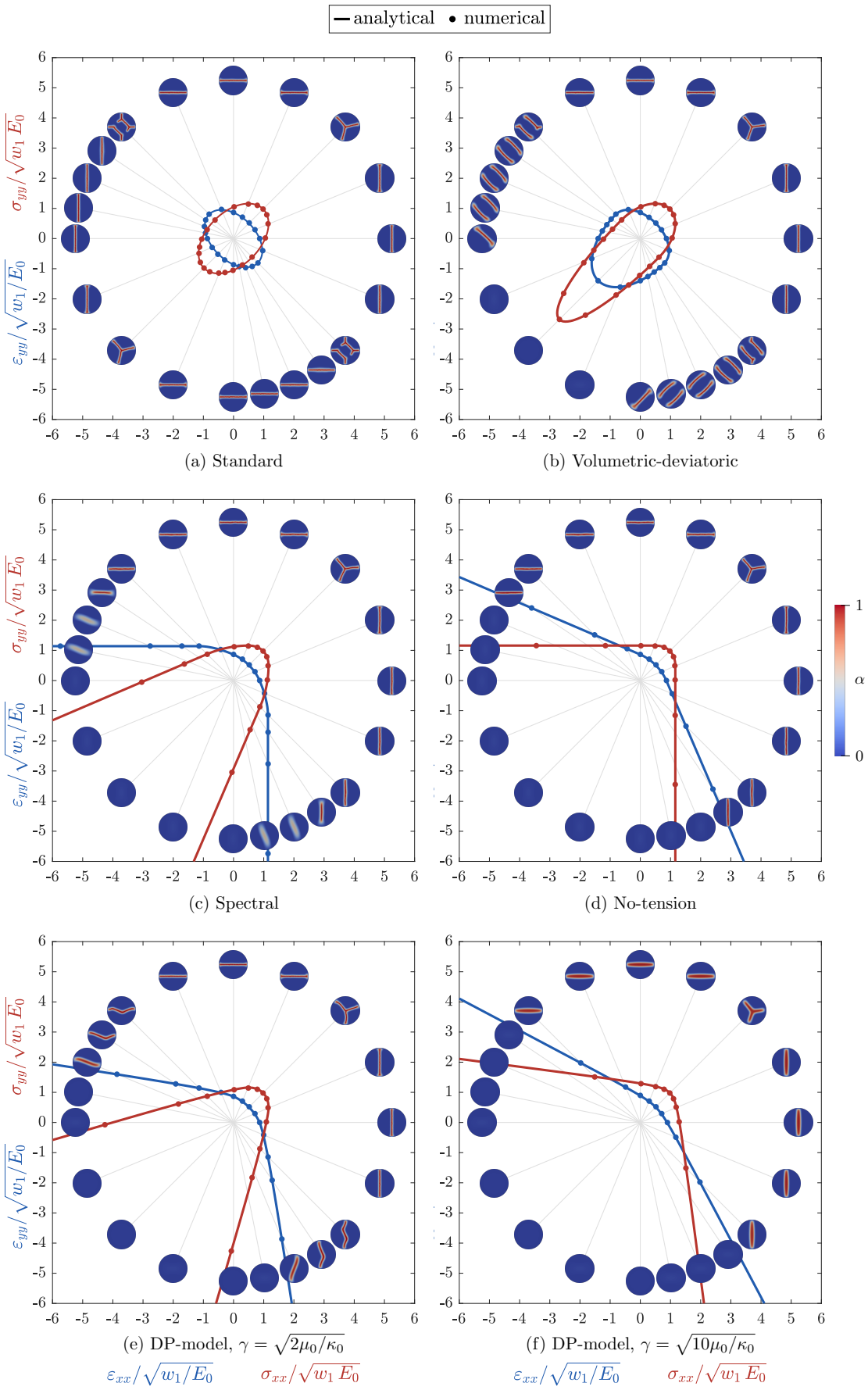


Fig. 12: Analytical (lines) versus numerical (dots) nucleation domains and damage fields after nucleation for the available models.

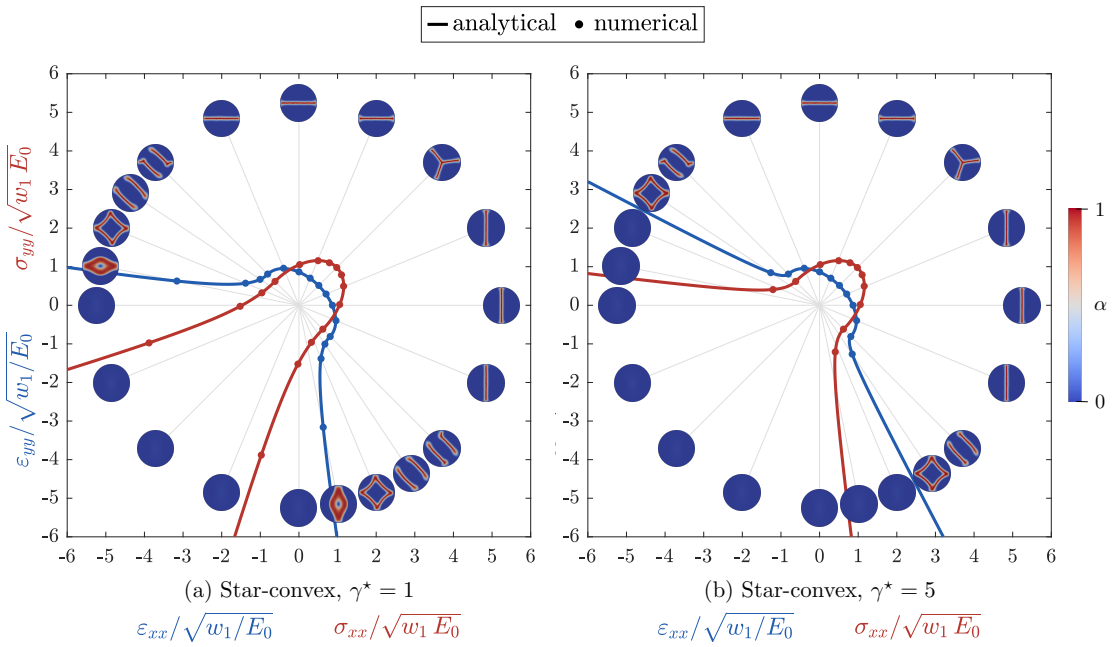


Fig. 13: Analytical (lines) versus numerical (dots) nucleation domains and damage fields after nucleation for the star-convex model.

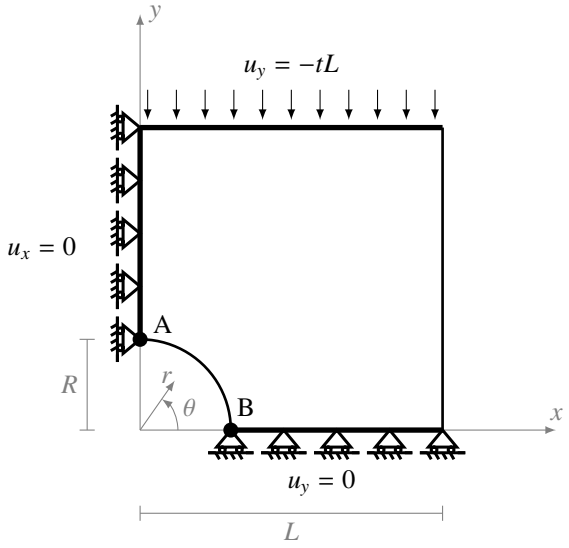


Fig. 14: Geometry and loading for the plate with hole.

$\sigma^{\mathrm{B}}_{\theta\theta} = -3\sigma^{\mathrm{A}}_{\theta\theta}$ [47], we can infer that if the $|\sigma^-_{\theta\theta_e}/\sigma^+_{\theta\theta_e}|$ ratio is well below 3, nucleation will occur in B, and if it is well above 3, it will occur in A (Table 3).

For the standard phase-field model, which has an elastic domain symmetric in tension and compression, damage starts at point B, as shown in Figure 16b. Additionally, the asymmetry alone is not sufficient to prevent crack initiation in B, as visible in Figures 16d, 16f and 17f as for these models the $|\sigma^-_{\theta\theta_e}/\sigma^+_{\theta\theta_e}|$ ratio is well below 3 (Tab. 3). Unlike the other models, the DP-like and the star-convex models contain the additional parameters $\gamma$ and $\gamma^\star$ that allow us for the flexible calibration the strength ratio $|\sigma^-_{\theta\theta_e}/\sigma^+_{\theta\theta_e}|$. For the star-convex model, Figure 15 shows how the $|\sigma^-_{\theta\theta_e}/\sigma^+_{\theta\theta_e}|$ ratio is affected by the variation of $\gamma^\star$.

Figures 16 and 17 present the results of the plate with hole test. For each model, we show the plot of the vertical stress reaction per unit thickness $R_y$, equal to the integral of $\sigma_{yy}$ over the upper boundary, against the pseudo-time $t$, as well as the damage field at the last time step. Some models do not reach iterative convergence of the numerical solver for all time steps; for these models, we report the results up to the last converged time step (a brief discussion on convergence issues is postponed to Section 5.4). In the $R_y$ vs. $t$ plots, the elastic limit point $e$ marks the transition between the elastic regime (black dash-dotted line) and the stage after damage nucleation (red solid line). From Figures 16a, 16c, 16e and 17e we observe that, in models for which nucleation occurs at point B, the elastic limit $e$ is met at different time steps. While the volumetric-deviatoric, spectral, and star-convex split with $\gamma^\star = 1$ introduce

| Model | $\lvert\sigma^-_{\theta\theta_e}/\sigma^+_{\theta\theta_e}\rvert$ | $\nu_0$=0.3 |
|---|---|---|
| Standard | 1 | =1 |
| Vol.-dev. | $\sqrt{\frac{3(1-\nu_0^2)}{2(1+\nu_0^3)}}$ | ≈1.15 |
| Spectral | $\frac{\sqrt{1-\nu_0-\nu_0^2}}{\nu_0}$ | ≈2.60 |
| No-tension | $\infty$ | =$\infty$ |
| DP-like | $\begin{cases} \frac{\sqrt{3(1-\nu_0)(\gamma_\infty\zeta+\gamma^2)}}{\sqrt{(1-2\nu_0)(1+\nu_0)(\gamma_\infty-\gamma)}} & \text{for} \quad \gamma<\zeta=\frac{3(1-2\nu_0)}{\gamma_\infty(1+\nu_0)} \\ \frac{\gamma_\infty+\gamma}{\gamma_\infty-\gamma} & \text{for} \quad \zeta\le\gamma<\gamma_\infty=\frac{\sqrt{6(1-\nu_0+\nu_0^2)}}{(1+\nu_0)} \\ \infty & \text{otherwise} \end{cases}$ | $\zeta$≈0.55<br>$\gamma_\infty$≈1.67 |
| Star-convex | $\begin{cases} \sqrt{\frac{\gamma^\star_\infty+1}{\gamma^\star_\infty-\gamma^\star}} & \text{for} \quad \gamma^\star<\gamma^\star_\infty=\frac{2(1+\nu_0^3)}{(1+\nu_0)^2(1-2\nu_0)} \\ \infty & \text{otherwise} \end{cases}$ | $\gamma^\star_\infty$≈3.04 |

Tab. 3: $\lvert\sigma^-_{\theta\theta_e}/\sigma^+_{\theta\theta_e}\rvert$ ratio for the plate with hole. With reference to Figure 14, first nucleation is expected in B when the ratio is well below 3. Nucleation is expected in A when the ratio is well above 3.

tension/compression asymmetry, this is not sufficient to obtain damage onset at point A. In the case of the spectral split in Figure 16f, the nucleation of the diffuse damage in B occurs before vertical localization at point A. Consequently, the nucleation point $e$ in Figure 16e corresponds to the initiation of damage in B. Thus, the only models that exhibit a crack propagation consistent with the experimental evidence [46] are those with a certain level of flexibility, adjustable with the parameter $\gamma$ (DP-like model) or $\gamma^\star$ (star-convex split), along with the no-tension model. However, in the case of the DP-like model (Figure 17d), for $\gamma = \sqrt{10\mu_0/\kappa_0}$, the damage exhibits a diffuse pattern rather than being fully localized. This is attributed to the phenomenon of crack thickening as $\gamma$ increases, as previously highlighted in the bi-axially loaded disk test.

### *5.3. Sliding test*

The last test concerns a square plate of side $L$ with a crack in the center, as shown in Figure 18, under plane-strain conditions. The bottom left corner of the plate coincides with the origin of the cartesian reference system $x$-$y$ and the out-of-plane direction is denoted with $z$. In order to emulate a crack using a localized damage field, we impose the Dirichlet boundary condition $\alpha(x, y = L/2) = 1$ and we solve the minimization problem (3) while maintaining the displacement field homogeneously equal to zero. Starting from the obtained damage field, we apply the Dirichlet boundary conditions in Figure 18 to the displacement field: the lower part of the plate is blocked in both directions and a horizontal displacement $u_x(x, y = L) = tL$ is applied to the upper part. Furthermore, the two sides are vertically blocked in their lower part $u_y(x = 0, y \le L/2) = u_y(x = L, y \le L/2) = 0$ and we apply a constant vertical displacement, i.e. independent of $t$, on the upper part $u_y(x = 0, y \ge L/2) = u_y(x = L, y \ge L/2) = \bar{u}L$, where $\bar{u} = 0.1$. This test aims to emphasize the importance of having zero residual shear stresses at full damage. Indeed, if these stresses are not zero, even though the two faces of the block are separate, physically unrealistic stresses are transmitted during sliding. This test is inspired by the one illustrated in [48] with additional separation of the two blocks. This excludes the possibility that the transmitted stresses are attributable to friction. We set $L = 1$, $E_0 = 100$, $\nu_0 = 0.3$, $w_1 = 1$ and $\ell = 0.05$. We discretize the problem with standard bilinear quadrilateral finite elements using a structured mesh with $h = \ell/5$.

Figure 19 depicts the deformed configuration at $t = 0.2$ for each model, except for the spectral and no-tension models, both of which experience convergence issues and thus stop at $t = 0.06$. The no-tension model and the DP-like model for $\gamma = \sqrt{10\mu_0/\kappa_0}$ in Figure 19d and 19f, respectively, display unrealistic deformations. Figure 20 illustrates for each model the horizontal stress reaction per unit thickness $R_x$, given by the integral of $\sigma_{xy}$ over the upper side of the plate, against $t$, compared to the horizontal elastic stress reaction of an undamaged plate (green dotted line). Given the presence of the crack and the initial separation, we expect the horizontal reaction force to be identically zero. However, this occurs only for the standard model, which has no residual stresses, and for the volumetric-deviatoric and the star-convex models, both of which have residual stresses proportional to $\langle \mathrm{tr}(\boldsymbol{\varepsilon})\rangle_-$. The spectral and the no-tension models, as well as the DP-like model for $\gamma = \sqrt{10\mu_0/\kappa_0}$, exhibit a significant reaction force, slightly lower than half of that observed in an undamaged material. The DP-like model for $\gamma = \sqrt{2\mu_0/\kappa_0}$ initially displays no reaction and a

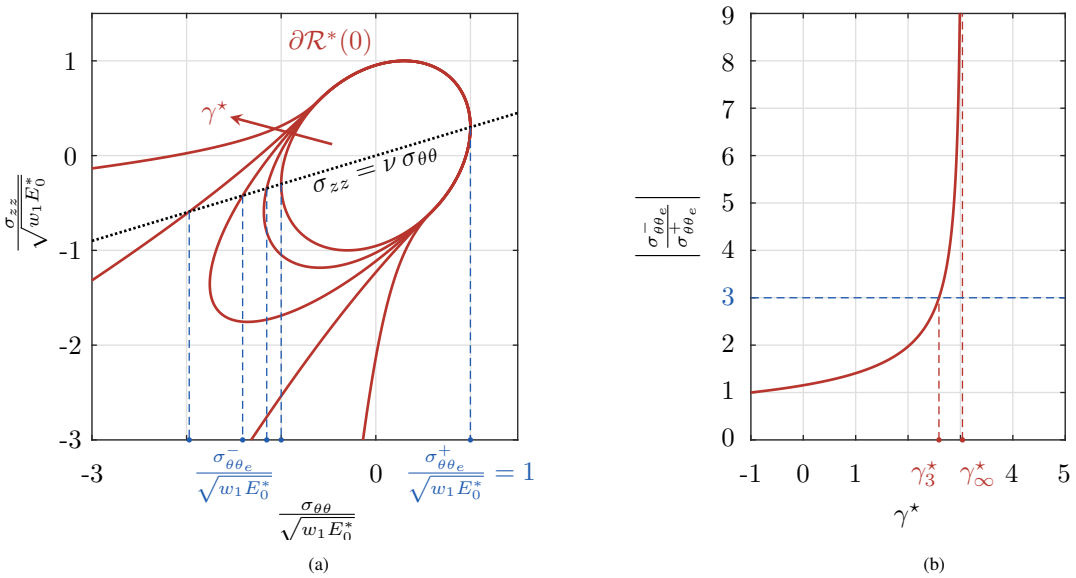


(a) (b)

Fig. 15: Effect of $\gamma^\star$ on the nucleation domain in the plane spanned by hoop stress and out-of-plane stress for the plate with hole test. Elastic limit hoop stresses (a): the red solid line and the black dashed line represent the contour $\partial\mathcal{R}^*(0)$ for $\gamma^\star = \{-1, 0, 1, 2, 5\}$ and the stress state under the plane-strain assumption, respectively. Their intersection determines the compressive limit $\sigma^-_{\theta\theta_e}$ (blue on the left) and the tensile limit $\sigma^+_{\theta\theta_e}$ (blue on the right). Compressive-tensile hoop limits ratio (b): trend of the limits ratio vs. $\gamma^\star$ (red solid line). For $\gamma^\star > \gamma_3^\star$ the ratio is greater than 3, for $\gamma^\star \geq \gamma_\infty^\star$ the ratio is equal to $\infty$.

deformation as shown in Figure 19, which is acceptable. However, it subsequently shows an increase in the reaction force. This is because a lower $\gamma$ value delays this undesired effect.

### *5.4. Iterative convergence issues*

As described in Section 5, the iterative convergence criterion of the alternate minimization is met when $R_u < \texttt{tol}$. Given the convexity of the functional in the separate problems of displacement and damage, the standard model is robust in terms of iterative convergence. However, due to the high non-linearity introduced by the energy decompositions, for the other models iterative convergence is often problematic. To achieve convergence, some authors [see e.g. 49] resort to non-variational simplified versions of the volumetric-deviatoric and spectral models, known as the hybrid model [44]. In fact, we already showed in Sections 5.2 and 5.3 that, for each model, we had to stop specific numerical tests at the first non-converging time step. The presented results exclusively relate to converged simulations. On the other hand, the same tests with modified parameters can lead to no convergence. In Figure 21, we illustrate the exemplary case of an angle $\theta$ in the bi-axially loaded disk test using the star-convex model, for which iterative convergence is lost when varying the mesh size $h$. This issue calls for a thorough numerical analysis addressing the specific non-linearities introduced by the splits. It is a crucial issue to be resolved for the proper numerical implementation of phase-field modeling of fracture under multi-axial stress states, but it goes beyond the scope of this work.

## 6. Conclusions

In this contribution, we focused on variational phase-field models for brittle fracture under multi-axial stress states based on energy decomposition. We first reviewed some available models of this type, namely the volumetric-deviatoric [13], the spectral [14], the no-tension [15] and the DP-like models [12]. We then proposed a new model that we denoted as star-convex model. The major contents and findings of the paper can be summarized as follows:

- We defined essential requirements for a phase-field model of brittle fracture dealing with multi-axial stress states (Sec 2.4): strain-hardening, stress-softening, tension/compression asymmetry, flexibility (i.e. the ability

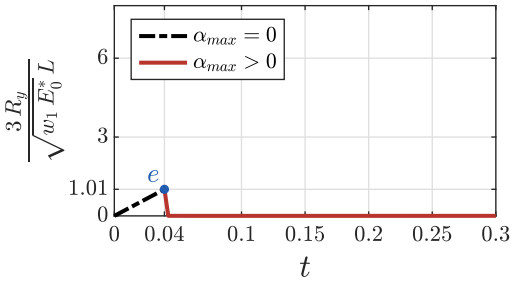


(a) Standard

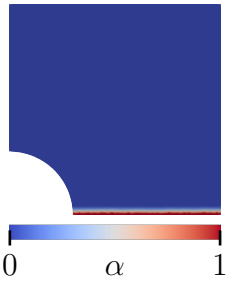


(b) Standard

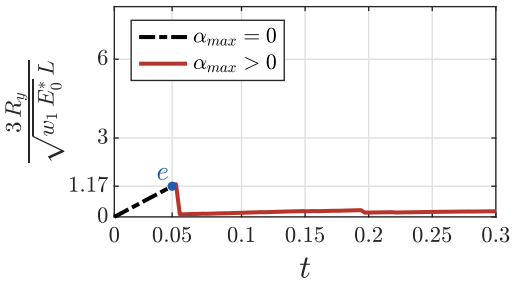


(c) Volumetric-deviatoric

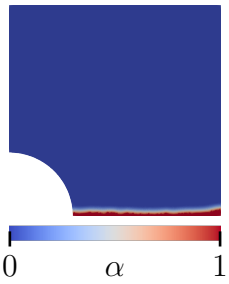


(d) Volumetric-deviatoric

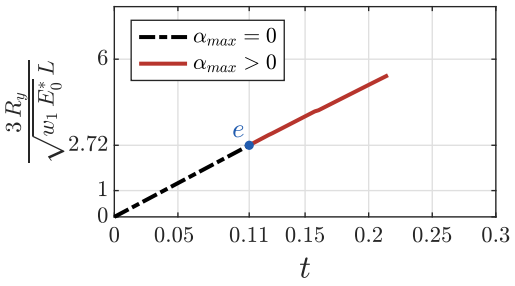


(e) Spectral

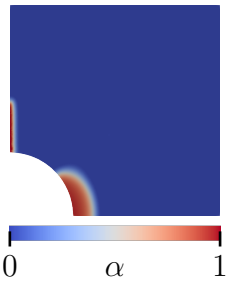


(f) Spectral

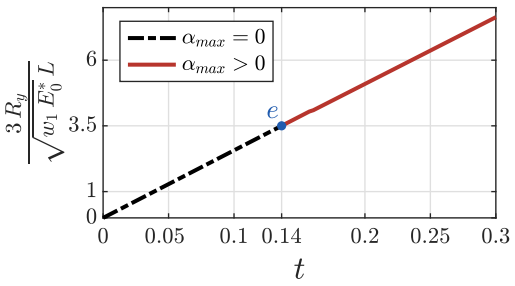


(g) No-tension

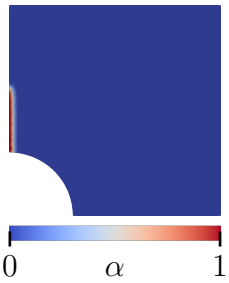


(h) No-tension

Fig. 16: Results of the plate with hole test for the standard, volumetric-deviatoric, spectral and no-tension models. Vertical reaction against pseudo-time $t$ (a), (c), (e), (g): the black dash-dotted line corresponds to the elastic phase, the $e$ point to damage nucleation and the red solid line to the post-nucleation phase. Damage fields (b), (d), (f), (h).

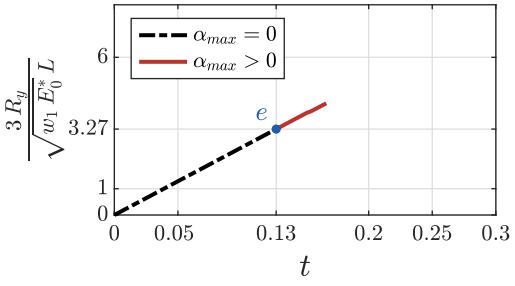


(a) DP-model, $\gamma = \sqrt{2\mu_0/\kappa_0}$

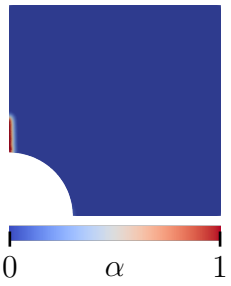


(b) DP-model, $\gamma = \sqrt{2\mu_0/\kappa_0}$

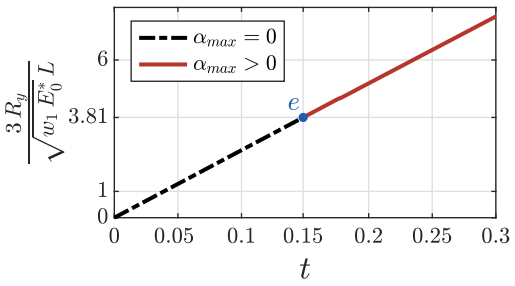


(c) DP-model, $\gamma = \sqrt{10\mu_0/\kappa_0}$

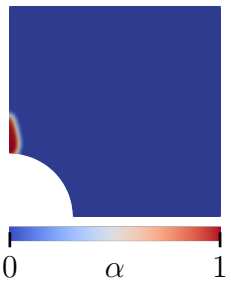


(d) DP-model, $\gamma = \sqrt{10\mu_0/\kappa_0}$

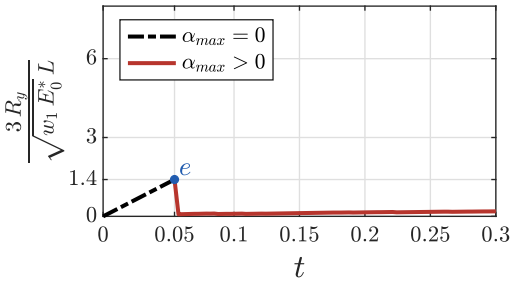


(e) Star-convex, $\gamma^\star = 1$

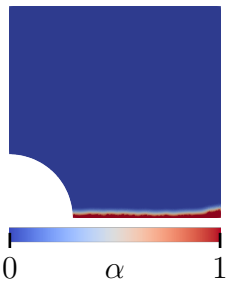


(f) Star-convex, $\gamma^\star = 1$

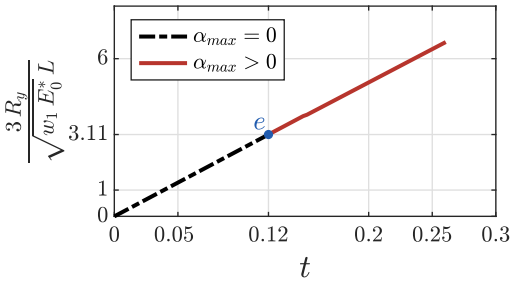


(g) Star-convex, $\gamma^\star = 5$

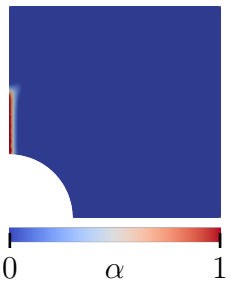


(h) Star-convex, $\gamma^\star = 5$

Fig. 17: Results of the plate with hole test for the DP-like ($\gamma = \{\sqrt{2\mu_0/\kappa_0}, \sqrt{10\mu_0/\kappa_0}\}$) and star-convex models ($\gamma^\star = \{1, 5\}$). Vertical reaction against pseudo-time $t$ (a), (c), (e), (g): the black dash-dotted line corresponds to the elastic phase, the $e$ point to damage nucleation and the red solid line to the post-nucleation phase. Damage fields (b), (d), (f), (h).

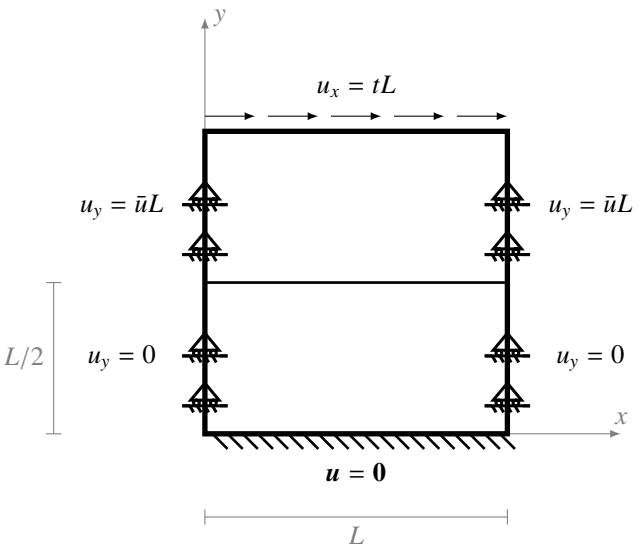


Fig. 18: Geometry and loading for the sliding test.

to independently calibrate not only the uniaxial tensile strength but also the uniaxial compressive strength and the shear strength), and crack-like residual stress.

- In light of these requirements we discussed the advantages and limitations of the available models. As summarized in Table 2, none of the analyzed existing decompositions was found to meet all the requirements.
- Our newly proposed star-convex model, based on a minimal modification of the volumetric-deviatoric decomposition, is equipped with a $\gamma^\star$ parameter that allows independent calibration of compressive and tensile strengths. Such partial flexibility can be extended to the shear strength by modifying the softening laws as analyzed in [37]. Additionally, the model satisfies all other requirements. Thus, it represents a very simple but effective step forward towards the realistic prediction of brittle fracture mechanisms under multiaxial stress states.

The issue of iterative convergence, which is crucial for the robustness of the simulations with all the presented models, remains open and may well be the topic of further investigations.

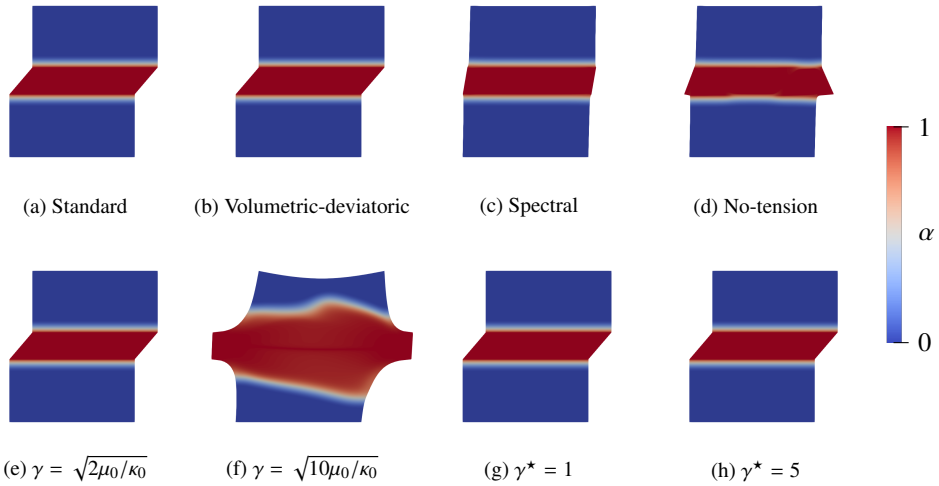


(a) Standard (b) Volumetric-deviatoric (c) Spectral (d) No-tension

(e) $\gamma = \sqrt{2\mu_0/\kappa_0}$ (f) $\gamma = \sqrt{10\mu_0/\kappa_0}$ (g) $\gamma^\star = 1$ (h) $\gamma^\star = 5$

Fig. 19: Damage fields on the deformed configurations for all models.

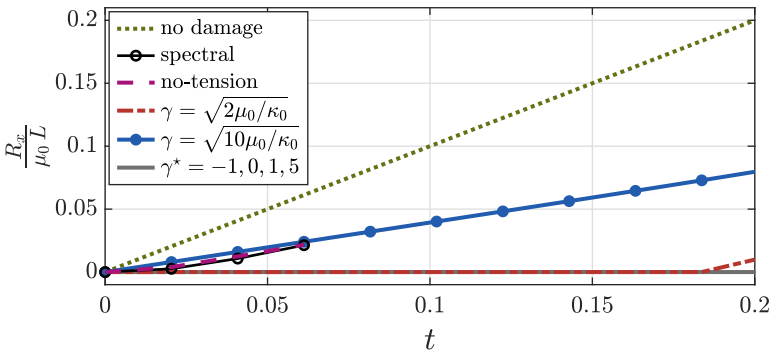


Fig. 20: Horizontal reaction vs. pseudo-time $t$ obtained from different models: linear elasticity (green dotted line) and phase-field models with spectral split (black solid line with empty circles), no-tension model (purple dashed line), DP-like model with $\gamma = \sqrt{2\mu_0/\kappa_0}$ (red dash-dotted line), DP-like model with $\gamma = \sqrt{10\mu_0/\kappa_0}$ (blue solid line with point marker). The grey solid line corresponds to the star-convex split with $\gamma^\star = \{1, 5\}$, to the volumetric-deviatoric split ($\gamma^\star = 0$) and to the standard model ($\gamma^\star = -1$).

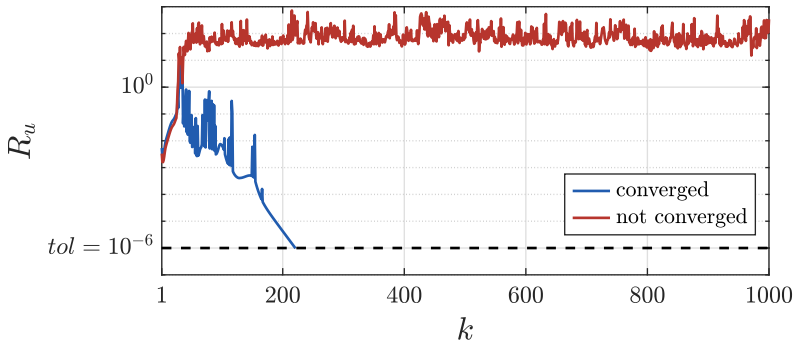


Fig. 21: Bi-axially loaded disk with the star-convex model $\left(\gamma^* = 1, \theta = \frac{3}{4}\pi\right)$: $R_u$ against iterations of the alternate minimization scheme for the time step at which the elastic limit is reached. All the parameters are as in Section 5.1 for the solid blue line $\left(h = \frac{\ell}{3}\right)$. For the solid red line, only the mesh size differs $\left(h = \frac{\ell}{5}\right)$.

## Appendix A. Elastic domains

In this section, we provide the expressions of the elastic domains for the models presented in Section 3.

*Appendix A.1. The volumetric-deviatoric split*

The elastic domains are

$$\mathcal{R}(\alpha) := \left\{ \boldsymbol{\varepsilon} \in \mathrm{Sym} : \frac{1}{2}\,\kappa_0\,\langle \mathrm{tr}(\boldsymbol{\varepsilon})\rangle_+^2 + \mu_0\,|\boldsymbol{\varepsilon}_{\mathrm{dev}}|^2 \leq -\frac{w_1 w'(\alpha)}{a'(\alpha)} \right\}, \tag{A.1}$$

$$\mathcal{R}^*(\alpha) := \left\{ \boldsymbol{\sigma} \in \mathrm{Sym} : \frac{1}{2n^2\kappa_0}\langle \mathrm{tr}(\boldsymbol{\sigma})\rangle_+^2 + \frac{1}{4\mu_0}|\boldsymbol{\sigma}_{\mathrm{dev}}|^2 \leq \frac{w_1 w'(\alpha)}{s'(\alpha)} \right\}. \tag{A.2}$$

*Appendix A.2. The spectral split*

The elastic domain in strains corresponds to

$$\mathcal{R}(\alpha) := \left\{ \boldsymbol{\varepsilon} \in \mathrm{Sym} : \frac{1}{2}\,\lambda_0\,\langle \mathrm{tr}(\boldsymbol{\varepsilon})\rangle_+^2 + \mu_0 \boldsymbol{\varepsilon}^+ \cdot \boldsymbol{\varepsilon}^+ \leq -\frac{w_1 w'(\alpha)}{a'(\alpha)} \right\}. \tag{A.3}$$

Assuming, without loss of generality, that $\sigma_1 \geq \sigma_2 \geq \sigma_3$ are the eigenvalues of the stress tensor $\boldsymbol{\sigma}$, the stress domain $\mathcal{R}^*(\alpha)$ is obtained as the set of $\boldsymbol{\sigma} \in Sym$ such that

– if $\sigma_3 - \nu_0(\sigma_1 + \sigma_2) \geq 0$

$$\frac{1}{18\kappa_0}\mathrm{tr}^2(\boldsymbol{\sigma}) + \frac{1}{4\mu_0}\,|\boldsymbol{\sigma}_{\mathrm{dev}}|^2 \leq \frac{w_1 w'(\alpha)}{s'(\alpha)},$$

– else if $[(1 + a(\alpha))\,\lambda_0 + 2\mu_0]\,\sigma_2 - \lambda_0\sigma_1 - a(\alpha)\,\lambda_0\sigma_3 \geq 0$ and $\sigma_1 + \sigma_2 + a(\alpha)\,\sigma_3 \geq 0$

$$\begin{aligned}
&\frac{1}{4a^2(\alpha)\,\mu_0\,[(2 + a(\alpha))\,\lambda_0 + 2\mu_0]^2} \\
&\Big\{4\mu_0^2\left(\sigma_1^2 + \sigma_2^2\right) + 2\lambda_0\mu_0\left[(3 + 2a(\alpha))\,\sigma_1^2 - 2\sigma_1\sigma_2 + (3 + 2a(\alpha))\,\sigma_2^2 + a^2(\alpha)\,\sigma_3^2\right] \\
&+\lambda_0^2\Big[\left(2 + 2a(\alpha) + a^2(\alpha)\right)\left(\sigma_1^2 + \sigma_2^2\right) - 2a^2(\alpha)\,\sigma_2\sigma_3 + 2a^2(\alpha)\,\sigma_3^2 \\
&-2\sigma_1\left(2\sigma_2 + 2a(\alpha)\,\sigma_2 + a^2(\alpha)\,\sigma_3\right)\Big]\Big\} \leq -\frac{w_1 w'(\alpha)}{a'(\alpha)},
\end{aligned}$$

– else if $[(1 + a(\alpha))\,\lambda_0 + 2a(\alpha)\,\mu_0]\,\sigma_2 - \lambda_0\sigma_1 - a(\alpha)\,\lambda_0\sigma_3 \geq 0$ and $\sigma_1 + \sigma_2 + a(\alpha)\,\sigma_3 \leq 0$

$$\begin{aligned}
&\frac{1}{4a^2(\alpha)\,\mu_0\,[(2 + a(\alpha))\,\lambda_0 + 2a(\alpha)\,\mu_0]^2} \\
&\Big\{\left[(\lambda_0 + a(\alpha)\,\lambda_0 + 2a(\alpha)\,\mu_0)\,\sigma_1 - \lambda_0\sigma_2 - a(\alpha)\,\lambda_0\sigma_3\right]^2 \\
&+\left[(\lambda_0 + a(\alpha)\,\lambda_0 + 2a(\alpha)\,\mu_0)\,\sigma_2 - \lambda_0\sigma_1 - a(\alpha)\,\lambda_0\sigma_3\right]^2\Big\} \leq -\frac{w_1 w'(\alpha)}{a'(\alpha)},
\end{aligned}$$

– else if $2\mu_0\sigma_1 + a(\alpha)\,\lambda_0\,(2\sigma_1 - \sigma_2 - \sigma_3) \geq 0$ and $\sigma_1 + a(\alpha)\,(\sigma_2 + \sigma_3) \geq 0$

$$\begin{aligned}
&\frac{1}{4a^2(\alpha)\,\mu_0\,[(1 + 2a(\alpha))\,\lambda_0 + 2\mu_0]^2}\Big\{\Big[(8a(\alpha) + 2)\,\lambda_0\mu_0 + 4\mu_0^2\Big]\,\sigma_1^2 \\
&+ a^2(\alpha)\,\lambda_0\left[2\mu_0\,(\sigma_2 + \sigma_3)^2 + \lambda_0\,(-2\sigma_1 + \sigma_2 + \sigma_3)^2\right]\Big\} \leq -\frac{w_1 w'(\alpha)}{a'(\alpha)},
\end{aligned}$$

– else if $2(\lambda_0+\mu_0)\sigma_1 - \lambda_0(\sigma_2+\sigma_3) \geq 0$ and $\sigma_1 + a(\alpha)(\sigma_2+\sigma_3) \leq 0$

$$\frac{1}{4\mu_0\left[(1+2a(\alpha))\lambda_0 + 2a(\alpha)\mu_0\right]^2}\left[2(\lambda_0+\mu_0)\sigma_1 - \lambda(\sigma_2+\sigma_3)\right]^2 \leq -\frac{w_1 w'(\alpha)}{a'(\alpha)}.$$

*Appendix A.3. The no-tension model*

In the case of no-tension materials, Freddi and Royer-Carfagni [15] define $\mathcal{K}_\varepsilon = \mathrm{Sym}^+$, the convex cone of symmetric positive semi-definite second-order tensors. The solution to the minimization problem (33) with $\mathcal{K}_\varepsilon = \mathrm{Sym}^+$ for the three-dimensional scenario is already presented in [50]. Assuming without loss of generality that the eigenvalues of $\boldsymbol{\varepsilon}$ are ordered such that $\varepsilon_1 \geq \varepsilon_2 \geq \varepsilon_3$ :

– if $\varepsilon_3 \geq 0$, then $\bar{\boldsymbol{\eta}} = \boldsymbol{\varepsilon}$,

– else if $\varepsilon_2 + \nu_0\varepsilon_3 \geq 0$, then $\bar{\eta}_1 = \varepsilon_1 + \nu_0\varepsilon_3$, $\bar{\eta}_2 = \varepsilon_2 + \nu_0\varepsilon_3$ and $\bar{\eta}_3 = 0$,

– else if $\varepsilon_1 + \frac{\nu_0}{1-\nu_0}(\varepsilon_2+\varepsilon_3) \geq 0$, then $\bar{\eta}_1 = \varepsilon_1 + \frac{\nu_0}{1-\nu_0}(\varepsilon_2+\varepsilon_3)$ and $\bar{\eta}_2 = \bar{\eta}_3 = 0$,

– else, $\bar{\boldsymbol{\eta}} = \mathbf{0}$.

Starting from $\varphi_D(\boldsymbol{\varepsilon})$, one can calculate the elastic domain $\mathcal{R}(\alpha)$ as the set of $\boldsymbol{\varepsilon} \in \mathrm{Sym}$ such that:

– if $\varepsilon_3 \geq 0$, $\frac{\kappa_0}{2}\mathrm{tr}^2(\boldsymbol{\varepsilon}) + \mu_0|\boldsymbol{\varepsilon}_{\mathrm{dev}}|^2 \leq -\frac{w_1 w'(\alpha)}{a'(\alpha)}$,

– else if $\varepsilon_2 + \nu_0\varepsilon_3 \geq 0$, $\frac{\lambda_0^2}{2(\lambda_0+\mu_0)}\varepsilon_3^2 + \lambda_0\varepsilon_3(\varepsilon_1+\varepsilon_2) + \frac{\lambda_0}{2}(\varepsilon_1+\varepsilon_2)^2 + \mu_0(\varepsilon_1^2+\varepsilon_2^2) \leq -\frac{w_1 w'(\alpha)}{a'(\alpha)}$,

– else if $\varepsilon_1 + \frac{\nu_0}{1-\nu_0}(\varepsilon_2+\varepsilon_3) \geq 0$, $\frac{1}{2(\lambda_0+2\mu_0)}\left[(\lambda_0+2\mu_0)\varepsilon_1 + \lambda_0(\varepsilon_2+\varepsilon_3)\right]^2 \leq -\frac{w_1 w'(\alpha)}{a'(\alpha)}$

and reversing the behavior law $\boldsymbol{\sigma}(\boldsymbol{\varepsilon}, \alpha)$ in (10), one can also derive the domain in the stresses $\mathcal{R}^*(\alpha)$ which is the set of $\boldsymbol{\sigma} \in \mathrm{Sym}$ such that:

– if $\sigma_3 - \nu_0(\sigma_1+\sigma_2) \geq 0$, $\frac{1}{18\kappa_0}\mathrm{tr}^2(\boldsymbol{\sigma}) + \frac{1}{4\mu_0}|\boldsymbol{\sigma}_{\mathrm{dev}}|^2 \leq \frac{w_1 w'(\alpha)}{s'(\alpha)}$,

– else if $\sigma_2 - \frac{\nu_0}{1-\nu_0}\sigma_1 \geq 0$, $\frac{1}{8\mu_0(\lambda_0+\mu_0)}\left[\lambda_0(\sigma_1-\sigma_2)^2 + 2\mu_0(\sigma_1^2+\sigma_2^2)\right] \leq \frac{w_1 w'(\alpha)}{s'(\alpha)}$,

– else if $\sigma_1 \geq 0$, $\frac{1}{2(\lambda_0+\mu_0)}\sigma_1^2 \leq \frac{w_1 w'(\alpha)}{s'(\alpha)}$.

*Appendix A.4. DP-like model*

Having defined $\mathcal{K}_\varepsilon$ and knowing the elastic energy density of the pristine material $\varphi_0(\boldsymbol{\varepsilon})$, one can solve the minimum problem in (33) as in [12], find

$$\bar{\boldsymbol{\eta}}(\boldsymbol{\varepsilon}) = \begin{cases} \boldsymbol{\varepsilon} & \text{for} \quad |\boldsymbol{\varepsilon}_{\mathrm{dev}}| < \mathrm{tr}(\boldsymbol{\varepsilon})/\gamma, \\ \mathbf{0} & \text{for} \quad |\boldsymbol{\varepsilon}_{\mathrm{dev}}| < -\frac{\gamma\kappa_0}{2\mu_0}\mathrm{tr}(\boldsymbol{\varepsilon}), \\ \frac{\mathrm{tr}(\boldsymbol{\varepsilon}) + \frac{2\mu_0}{\kappa_0\gamma}|\boldsymbol{\varepsilon}_{\mathrm{dev}}|}{\gamma + \frac{2\mu_0}{\kappa_0\gamma}}\left(\frac{\gamma}{n}\mathbf{I} + \hat{\boldsymbol{\varepsilon}}_{\mathrm{dev}}\right) & \text{for} \quad |\boldsymbol{\varepsilon}_{\mathrm{dev}}| \geq \mathrm{tr}(\boldsymbol{\varepsilon})/\gamma \;\&\; |\boldsymbol{\varepsilon}_{\mathrm{dev}}| \geq -\frac{\gamma\kappa_0}{2\mu_0}\mathrm{tr}(\boldsymbol{\varepsilon}) \end{cases} \tag{A.4}$$

and obtain the elastic energy density split

$$\varphi_D(\boldsymbol{\varepsilon}) = \begin{cases} \frac{\kappa_0}{2}\mathrm{tr}^2(\boldsymbol{\varepsilon}) + \mu_0|\boldsymbol{\varepsilon}_{\mathrm{dev}}|^2 & \text{for} \quad |\boldsymbol{\varepsilon}_{\mathrm{dev}}| < \mathrm{tr}(\boldsymbol{\varepsilon})/\gamma, \\ 0 & \text{for} \quad |\boldsymbol{\varepsilon}_{\mathrm{dev}}| < -\frac{\gamma\kappa_0}{2\mu_0}\mathrm{tr}(\boldsymbol{\varepsilon}), \\ \frac{1}{2(\kappa_0\gamma^2+2\mu_0)}\left[\kappa_0\gamma\mathrm{tr}(\boldsymbol{\varepsilon}) + 2\mu_0|\boldsymbol{\varepsilon}_{\mathrm{dev}}|\right]^2 & \text{for} \quad |\boldsymbol{\varepsilon}_{\mathrm{dev}}| \geq \mathrm{tr}(\boldsymbol{\varepsilon})/\gamma \;\&\; |\boldsymbol{\varepsilon}_{\mathrm{dev}}| \geq -\frac{\gamma\kappa_0}{2\mu_0}\mathrm{tr}(\boldsymbol{\varepsilon}), \end{cases} \tag{A.5}$$

$$\varphi_R(\boldsymbol{\varepsilon}) = \begin{cases} 0 & \text{for} \quad |\boldsymbol{\varepsilon}_{\mathrm{dev}}| < \mathrm{tr}(\boldsymbol{\varepsilon})/\gamma, \\ \frac{\kappa_0}{2}\mathrm{tr}^2(\boldsymbol{\varepsilon}) + \mu_0|\boldsymbol{\varepsilon}_{\mathrm{dev}}|^2 & \text{for} \quad |\boldsymbol{\varepsilon}_{\mathrm{dev}}| < -\frac{\gamma\kappa_0}{2\mu_0}\mathrm{tr}(\boldsymbol{\varepsilon}), \\ \frac{\kappa_0\mu_0}{\kappa_0\gamma^2+2\mu_0}\left[\mathrm{tr}(\boldsymbol{\varepsilon}) - \gamma|\boldsymbol{\varepsilon}_{\mathrm{dev}}|\right]^2 & \text{for} \quad |\boldsymbol{\varepsilon}_{\mathrm{dev}}| \geq \mathrm{tr}(\boldsymbol{\varepsilon})/\gamma \;\&\; |\boldsymbol{\varepsilon}_{\mathrm{dev}}| \geq -\frac{\gamma\kappa_0}{2\mu_0}\mathrm{tr}(\boldsymbol{\varepsilon}). \end{cases} \tag{A.6}$$

The elastic domain in strains $\mathcal{R}(\alpha)$ is the set of $\boldsymbol{\varepsilon} \in \mathrm{Sym}$ such that:

– if $\mathrm{tr}(\boldsymbol{\varepsilon}) - \gamma|\boldsymbol{\varepsilon}_{\mathrm{dev}}| > 0$, $\frac{\kappa_0}{2}\mathrm{tr}^2(\boldsymbol{\varepsilon}) + \mu_0|\boldsymbol{\varepsilon}_{\mathrm{dev}}|^2 \leq -\frac{w_1 w'(\alpha)}{a'(\alpha)}$,

– else if $\mathrm{tr}(\boldsymbol{\varepsilon}) + \frac{2\mu_0}{\gamma\kappa_0}|\boldsymbol{\varepsilon}_{\mathrm{dev}}| \geq 0$, $\frac{1}{2(\kappa_0\gamma^2+2\mu_0)}\left[\kappa_0\gamma\mathrm{tr}(\boldsymbol{\varepsilon}) + 2\mu_0|\boldsymbol{\varepsilon}_{\mathrm{dev}}|\right]^2 \leq -\frac{w_1 w'(\alpha)}{a'(\alpha)}$.

The elastic domain in stresses $\mathcal{R}^*(\alpha)$ is the set of $\boldsymbol{\varepsilon} \in \mathrm{Sym}$ such that:

– if $\mathrm{tr}(\boldsymbol{\sigma}) - \frac{n\gamma\kappa_0}{2\mu_0}|\boldsymbol{\sigma}_{\mathrm{dev}}| > 0$, $\frac{\mathrm{tr}^2(\boldsymbol{\sigma})}{2n^2\kappa_0} + \frac{|\boldsymbol{\sigma}_{\mathrm{dev}}|^2}{4\mu_0} \leq \frac{w_1 w'(\alpha)}{s'(\alpha)}$,

– else if $\mathrm{tr}(\boldsymbol{\sigma}) + \frac{n}{\gamma}|\boldsymbol{\sigma}_{\mathrm{dev}}| \geq 0$, $\frac{1}{2n^2(\kappa_0\gamma^2+2\mu_0)}\left[\gamma\mathrm{tr}(\boldsymbol{\sigma}) + n|\boldsymbol{\sigma}_{\mathrm{dev}}|\right]^2 \leq \frac{w_1 w'(\alpha)}{s'(\alpha)}$.

## Appendix B. Conic sections

In this section, a procedure for the construction of a strain energy density which satisfies the requirements illustrated in Section 2.4 is proposed. First, we assume that the elastic domain is axisymmetric around the hydrostatic axis, hence it is sufficient to develop the model construction on the $\mathrm{tr}(\boldsymbol{\varepsilon})$ - $|\boldsymbol{\varepsilon}_{\mathrm{dev}}|$ plane. For the strain energy density $W(\boldsymbol{\varepsilon}, \alpha, \nabla\alpha)$, we keep the definition in (1) and, regarding local dissipation, we simply opt for the AT1-like function $w(\alpha) = \alpha$ that guarantees the existence of an initial linear elastic regime.

Since the energy density must be quadratic in $\boldsymbol{\varepsilon}$ for $\alpha = 0$, a simple functional candidate is the second-order polynomial in $\mathrm{tr}(\boldsymbol{\varepsilon})$ and $|\boldsymbol{\varepsilon}_{\mathrm{dev}}|$

$$\varphi(\boldsymbol{\varepsilon}, \alpha) = \frac{1}{2}\kappa(\alpha)\mathrm{tr}(\boldsymbol{\varepsilon})^2 + \mu(\alpha)|\boldsymbol{\varepsilon}_{\mathrm{dev}}|^2 + p(\alpha)\,\mathrm{tr}(\boldsymbol{\varepsilon}). \tag{B.1}$$

where in order to ensure smoothness of the elastic domain the linear term in $|\boldsymbol{\varepsilon}_{\mathrm{dev}}|$ is not included. The choice of a null coefficient for the mixed-term $\mathrm{tr}(\boldsymbol{\varepsilon})\,|\boldsymbol{\varepsilon}_{\mathrm{dev}}|$ in the polynomial aims to avoid complicated loss of coaxiality between strain and stress. In fact, the mixed-term allows the volumetric (deviatoric) stress to work for the deviatoric (volumetric) strain. Such constitutive laws are exemplified by the DP-like model and lead to undesired and convoluted residual stresses as illustrated in Section 3.4. Moreover, we assume that $\kappa(0) = \kappa_0$, $\mu(0) = \mu_0$, $p(0) = 0$ to retrieve classical linear elasticity for $\alpha = 0$. The constitutive law is obtained by work conjugacy, hence

$$\frac{\mathrm{tr}(\boldsymbol{\sigma})}{n} = \kappa(\alpha)\mathrm{tr}(\boldsymbol{\varepsilon}) + p(\alpha) \qquad \text{and} \qquad |\boldsymbol{\sigma}_{\mathrm{dev}}| = 2\,\mu(\alpha)\,|\boldsymbol{\varepsilon}_{\mathrm{dev}}|, \tag{B.2}$$

from which we see that $p(\alpha)$ acts as a pre-stress along the volumetric component.

The boundary of the elastic domain in the strain space is the set $\partial\mathcal{R}(\alpha)$ of $\boldsymbol{\varepsilon} \in \mathrm{Sym}$ such that

$$\frac{1}{2}\kappa'(\alpha)\mathrm{tr}(\boldsymbol{\varepsilon})^2 + \mu'(\alpha)|\boldsymbol{\varepsilon}_{\mathrm{dev}}|^2 + p'(\alpha)\mathrm{tr}(\boldsymbol{\varepsilon}) + w_1 = 0, \tag{B.3}$$

which is the implicit equation of a conic section in the $\mathrm{tr}(\boldsymbol{\varepsilon})$ - $|\boldsymbol{\varepsilon}_{\mathrm{dev}}|$ plane. The shape of the conic section is determined by the sign of the product $\kappa'(\alpha)\mu'(\alpha)$. Specifically, when the product is positive, zero or negative the conic section is respectively an ellipse, a parabola, or a hyperbola. It can be proved easily that the same shape is preserved by passing to the space of stresses, i.e., if $\partial\mathcal{R}(\alpha)$ is an ellipse, a parabola, or a hyperbola, then $\partial\mathcal{R}^*(\alpha)$ will be an ellipse, a parabola, or a hyperbola, respectively.

At least for $\mathrm{tr}(\boldsymbol{\varepsilon}) \geq 0$, a standard damaging behavior and finite elastic limits for $\alpha < 1$ are required, that is $\kappa(1) = 0$ and $\mu(1) = 0$ with $\kappa'(\alpha) \leq 0$, $p'(\alpha) \neq 0$ if $\kappa'(\alpha) = 0$ and $\mu'(\alpha) < 0$ for $\alpha < 1$. As a consequence, the boundary of the elastic domain can be either a parabola or an ellipse. A parabolic domain seems to hold distinct advantages, as it appears capable of describing infinite elastic limit in volumetric compression. On the other hand, within the interval $[0, 1]$ there is at least one $\alpha$ value for which the product $\kappa'(\alpha)\mu'(\alpha)$ is negative and, consequently, $\partial\mathcal{R}(\alpha)$ is an ellipse. The elastic domain adapts with $\alpha$, eventually morphing from an ellipse to a parabola. However, this morphing cannot occur in the reverse direction, from parabola to ellipse, without violating the strain-hardening condition. Consequently, fulfillment of strain-hardening requires that, for $\alpha = 0$, the elastic domain takes an elliptic shape. This constraint would confine us to models in which, under significant compressive loads, the deviatoric elastic limit decreases as volumetric compression increases, and this is a trend contrary to the models of our primary interest, such as the Drucker-Prager model.

Since the requirements on $\mathrm{tr}(\boldsymbol{\varepsilon}) \geq 0$ are more demanding, the split of the strain energy density

$$\varphi(\boldsymbol{\varepsilon}, \alpha) = \begin{cases} \frac{1}{2}\kappa_+(\alpha)\mathrm{tr}(\boldsymbol{\varepsilon})^2 + \mu(\alpha)|\boldsymbol{\varepsilon}_{\mathrm{dev}}|^2 + p(\alpha)\,\mathrm{tr}(\boldsymbol{\varepsilon}), & \text{if } \mathrm{tr}(\boldsymbol{\varepsilon}) \geq 0, \\ \frac{1}{2}\kappa_-(\alpha)\mathrm{tr}(\boldsymbol{\varepsilon})^2 + \mu(\alpha)|\boldsymbol{\varepsilon}_{\mathrm{dev}}|^2 + p(\alpha)\,\mathrm{tr}(\boldsymbol{\varepsilon}), & \text{if } \mathrm{tr}(\boldsymbol{\varepsilon}) < 0 \end{cases} \tag{B.4}$$

offers flexibility to the shape of the elastic domain at least for $\mathrm{tr}(\boldsymbol{\varepsilon}) < 0$. In (B.4), $\mu(\alpha)$ does not depend on the sign of $\mathrm{tr}(\boldsymbol{\varepsilon})$ to guarantee smoothness of the elastic domain. Also $p(\alpha)$ does not depend on the sign of $\mathrm{tr}(\boldsymbol{\varepsilon})$ to preserve the continuity of the elastic domain in the stress space. However, although selecting an independent $p(\alpha)$ from $\mathrm{tr}(\boldsymbol{\varepsilon})$ ensures continuity, this alone is insufficient to ensure smoothness of the elastic domain in the stress space. In addition to this, for $\mathrm{tr}(\boldsymbol{\varepsilon}) \geq 0$ it must be $p(0) = p(1) = 0$ to recover linear elasticity at $\alpha = 0$ and to obtain zero residual stresses at $\alpha = 1$. Consequently, there are inevitably values of $\alpha$ for which the elastic domain for $\mathrm{tr}(\boldsymbol{\varepsilon}) \geq 0$ is an ellipse with a center shifted to $\mathrm{tr}(\boldsymbol{\varepsilon}) > 0$. For this value of $\alpha$ then, as we approach $\mathrm{tr}(\boldsymbol{\varepsilon}) = 0$ from above, i.e. at the limit $\mathrm{tr}(\boldsymbol{\varepsilon}) \to 0^+$, there is a reduction in the deviatoric elastic limit with decreasing $\mathrm{tr}(\boldsymbol{\varepsilon})$ value, which once again contradicts the ideal behavior we aim to model. This complexity leads to exclude the translation effect in the case with energy split, i.e. $p(\alpha) = 0$.

At this point, a straightforward choice for $\mu(\alpha)$ is the standard one $\mu(\alpha) = \mu_0\,(1-\alpha)^2$. For a comprehensive analysis on the influence of different $\kappa(\alpha)$ functions on the elastic domain, we refer interested readers to [37]. For our current aim, it is worth noting that different choices of $\kappa(\alpha)$, as long as they follow stability rules and strain-hardening, provide only limited control over strength limits. Therefore, we opt for the simplest choice $\kappa_+(\alpha) = \kappa_0\,(1-\alpha)^2$.

Because of the split, the constraints on $\kappa_-(\alpha)$ are relaxed, so we can take $\kappa'(\alpha) > 0$, thus having hyperbolas on $\mathrm{tr}(\boldsymbol{\varepsilon}) < 0$ and a $\mathbf{0}$-star-convex elastic domain. In the $\mathrm{tr}(\boldsymbol{\varepsilon})$-$|\boldsymbol{\varepsilon}_{\mathrm{dev}}|$ plane, the hyperbola for $\mathrm{tr}(\boldsymbol{\varepsilon}) < 0$ has an asymptote

$$\frac{|\boldsymbol{\varepsilon}_{\mathrm{dev}}|}{\mathrm{tr}(\boldsymbol{\varepsilon})} = -\sqrt{\frac{\kappa'_-(\alpha)}{2\,(1-\alpha)}}. \tag{B.5}$$

Since for numerical robustness we prefer not to have a vertical asymptote for $\alpha \to 1$, a convenient choice is that of an asymptote with a slope independent of $\alpha$ and proportional to the root of a flexible parameter $\gamma^\star$, i.e., $\kappa(\alpha) = \kappa_0\left(1 + 2\,\gamma^\star\,\alpha\left(1 - \frac{\alpha}{2}\right)\right)$. In this manner, we construct the star-convex model

$$\varphi(\boldsymbol{\varepsilon}, \alpha) = \kappa_0\left(1 + 2\,\gamma^\star\,\alpha\left(1 - \frac{\alpha}{2}\right)\right)\mathrm{tr}(\boldsymbol{\varepsilon})^2 + \mu_0\,(1-\alpha)^2\,|\boldsymbol{\varepsilon}_{\mathrm{dev}}|^2, \tag{B.6}$$

$$\varphi(\boldsymbol{\varepsilon}, \alpha) = \begin{cases} \kappa_0\,(1-\alpha)^2\,\mathrm{tr}(\boldsymbol{\varepsilon})^2 + \mu_0\,(1-\alpha)^2\,|\boldsymbol{\varepsilon}_{\mathrm{dev}}|^2, & \text{if } \mathrm{tr}(\boldsymbol{\varepsilon}) \geq 0, \\ \kappa_0\left(1 + 2\,\gamma^\star\,\alpha\left(1 - \frac{\alpha}{2}\right)\right)\mathrm{tr}(\boldsymbol{\varepsilon})^2 + \mu_0\,(1-\alpha)^2\,|\boldsymbol{\varepsilon}_{\mathrm{dev}}|^2, & \text{if } \mathrm{tr}(\boldsymbol{\varepsilon}) < 0 \end{cases} \tag{B.7}$$

which, written in the canonical split form, is equivalent to (35).


## Acknowledgements

This research has received funding from the European Union's Horizon 2020 research and innovation programme under the Marie Skłodowska-Curie grant agreement No. 861061 – NEWFRAC Project.

This work was performed using HPC resources from GENCI-IDRIS (Grant 2023-AD010913451R1)


## References


[1] G. A. Francfort, J.-J. Marigo, Revisiting brittle fracture as an energy minimization problem, Journal of the Mechanics and Physics of Solids 46 (8) (1998) 1319–1342.

[2] B. Bourdin, G. A. Francfort, J.-J. Marigo, Numerical experiments in revisited brittle fracture, Journal of the Mechanics and Physics of Solids 48 (4) (2000) 797–826.

[3] L. Ambrosio, On the approximation of free discontinuity problems, Boll. Un. Mat. Ital., B (7) (1992) 105–123.

[4] K. Pham, H. Amor, J.-J. Marigo, C. Maurini, Gradient damage models and their use to approximate brittle fracture, International Journal of Damage Mechanics 20 (4) (2011) 618–652.

[5] J.-J. Marigo, C. Maurini, K. Pham, An overview of the modelling of fracture by gradient damage models 51 (12) 3107–3128. doi:10.1007/s11012-016-0538-4.
URL http://dx.doi.org/10.1007/s11012-016-0538-4
[6] B. Bourdin, G. A. Francfort, J.-J. Marigo, The variational approach to fracture, Journal of elasticity 91 (2008) 5–148.
[7] M. Negri, A comparative analysis on variational models for quasi-static brittle crack propagation (2010).
[8] A. A. L. Baldelli, C. Maurini, Numerical bifurcation and stability analysis of variational gradient-damage models for phase-field fracture, Journal of the Mechanics and Physics of Solids 152 (2021) 104424.
[9] E. Tanné, T. Li, B. Bourdin, J.-J. Marigo, C. Maurini, Crack nucleation in variational phase-field models of brittle fracture, Journal of the Mechanics and Physics of Solids 110 (2018) 80–99.
[10] T. Wu, A. Carpiuc, M. Poncelet, L. De Lorenzis, Phase-field simulation of interactive mixed-mode fracture tests on cement mortar with full-field displacement boundary conditions 182 658–688.
[11] A. Kumar, B. Bourdin, G. A. Francfort, O. Lopez-Pamies, Revisiting nucleation in the phase-field approach to brittle fracture, Journal of the Mechanics and Physics of Solids 142 (2020) 104027.
[12] L. De Lorenzis, C. Maurini, Nucleation under multi-axial loading in variational phase-field models of brittle fracture, International Journal of Fracture 237 (1-2) (2022) 61–81.
[13] H. Amor, J.-J. Marigo, C. Maurini, Regularized formulation of the variational brittle fracture with unilateral contact: Numerical experiments, Journal of the Mechanics and Physics of Solids 57 (8) (2009) 1209–1229.
[14] C. Miehe, F. Welschinger, M. Hofacker, Thermodynamically consistent phase-field models of fracture: Variational principles and multi-field fe implementations, International journal for numerical methods in engineering 83 (10) (2010) 1273–1311.
[15] F. Freddi, G. Royer-Carfagni, Regularized variational theories of fracture: a unified approach, Journal of the Mechanics and Physics of Solids 58 (8) (2010) 1154–1174.
[16] F. Freddi, G. Royer-Carfagni, Variational fracture mechanics to model compressive splitting of masonry-like materials, Annals of Solid and Structural Mechanics 2 (2011) 57–67.
[17] Y. Navidtehrani, C. Betegon, E. Martinez-Paneda, A general framework for decomposing the phase field fracture driving force, particularised to a drucker–prager failure surface, Theoretical and Applied Fracture Mechanics 121 (2022) 103555.
[18] N. P. van Dijk, J. J. Espadas-Escalante, P. Isaksson, Strain energy density decompositions in phase-field fracture theories for orthotropy and anisotropy, International Journal of Solids and Structures 196 (2020) 140–153.
[19] Q.-C. He, Q. Shao, Closed-form coordinate-free decompositions of the two-dimensional strain and stress for modeling tension–compression dissymmetry, Journal of Applied Mechanics 86 (3) (2019) 031007.
[20] B.-T. Vu, H. Le Quang, Q.-C. He, Modelling and simulation of fracture in anisotropic brittle materials by the phase-field method with novel strain decompositions, Mechanics Research Communications 124 (2022) 103936.
[21] E. Lorentz, A nonlocal damage model for plain concrete consistent with cohesive fracture, International Journal of Fracture 207 (2) (2017) 123–159.
[22] J. Ulloa, J. Wambacq, R. Alessi, E. Samaniego, G. Degrande, S. Francois, A micromechanics-based variational phase-field model for fracture in geomaterials with brittle-tensile and compressive-ductile behavior, Journal of the Mechanics and Physics of Solids 159 (2022) 104684.
[23] T. You, Q.-Z. Zhu, P.-F. Li, J.-F. Shao, Incorporation of tension-compression asymmetry into plastic damage phase-field modeling of quasi brittle geomaterials, International Journal of Plasticity 124 (2020) 71–95.
[24] F. Fei, J. Choo, Double-phase-field formulation for mixed-mode fracture in rocks, Computer Methods in Applied Mechanics and Engineering 376 (2021) 113655.
[25] M. Hakimzadeh, V. Agrawal, K. Dayal, C. Mora-Corral, Phase-field finite deformation fracture with an effective energy for regularized crack face contact, Journal of the Mechanics and Physics of Solids 167 (2022) 104994.
[26] C. Steinke, M. Kaliske, A phase-field crack model based on directional stress decomposition, Computational Mechanics 63 (2019) 1019–1046.
[27] J. Storm, D. Supriatna, M. Kaliske, The concept of representative crack elements for phase-field fracture: Anisotropic elasticity and thermo-elasticity, International Journal for Numerical Methods in Engineering 121 (5) (2020) 779–805.
[28] C. Miehe, L.-M. Schaenzel, H. Ulmer, Phase field modeling of fracture in multi-physics problems. part i. balance of crack surface and failure criteria for brittle crack propagation in thermo-elastic solids, Computer Methods in Applied Mechanics and Engineering 294 (2015) 449–485.
[29] X. Zhang, S. W. Sloan, C. Vignes, D. Sheng, A modification of the phase-field model for mixed mode crack propagation in rock-like materials, Computer Methods in Applied Mechanics and Engineering 322 (2017) 123–136.
[30] Y. Feng, J. Li, Phase-field method with additional dissipation force for mixed-mode cohesive fracture, Journal of the Mechanics and Physics of Solids 159 (2022) 104693.
[31] T. Wang, X. Ye, Z. Liu, D. Chu, Z. Zhuang, Modeling the dynamic and quasi-static compression-shear failure of brittle materials by explicit phase field method, Computational Mechanics 64 (2019) 1537–1556.
[32] S. Abrari Vajari, M. Neuner, P. K. Arunachala, C. Linder, Investigation of driving forces in a phase field approach to mixed mode fracture of concrete, Computer Methods in Applied Mechanics and Engineering 417 (2023) 116404.
[33] J.-J. Marigo, Constitutive relations in plasticity, damage and fracture mechanics based on a work property, Nuclear Engineering and Design 114 (3) (1989) 249–272.
[34] K. Pham, J.-J. Marigo, Approche variationnelle de l'endommagement : I. Les concepts fondamentaux, Comptes Rendus. Mécanique 338 (4) (2010) 191–198. doi:10.1016/j.crme.2010.03.009.
[35] K. Pham, J.-J. Marigo, C. Maurini, The issues of the uniqueness and the stability of the homogeneous response in uniaxial tests with gradient damage models, Journal of the Mechanics and Physics of Solids 59 (6) (2011) 1163–1190.
[36] K. Pham, J.-J. Marigo, Stability of homogeneous states with gradient damage models: size effects and shape effects in the three-dimensional setting, Journal of Elasticity 110 (2013) 63–93.
[37] C. Zolesi, C. Maurini, Crack nucleation in variational phase-field models of fracture with softening modulation, in progress (2023).
[38] A. Chambolle, S. Conti, G. A. Francfort, Approximation of a brittle fracture energy with a constraint of non-interpenetration, Archive for

Rational Mechanics and Analysis 228 (3) (2018) 867–889.
[39] G. Del Piero, D. R. Owen, Structured deformations of continua, Archive for Rational Mechanics and Analysis 124 (1993) 99–99.
[40] G. Lancioni, G. Royer-Carfagni, The variational approach to fracture mechanics. a practical application to the french panthéon in paris, Journal of elasticity 95 (2009) 1–30.
[41] G. Hansen, I. Herburt, H. Martini, M. Moszyńska, Starshaped sets, Aequationes mathematicae 94 (2020) 1001–1092.
[42] M. W. Scroggs, I. A. Baratta, C. N. Richardson, G. N. Wells, Basix: a runtime finite element basis evaluation library, Journal of Open Source Software 7 (73) (2022) 3982.
[43] M. W. Scroggs, J. S. Dokken, C. N. Richardson, G. N. Wells, Construction of arbitrary order finite element degree-of-freedom maps on polygonal anfd polyhedral cell meshes, ACM Transactions on Mathematical Software 48 (2) (2022) 18:1–18:23.
[44] M. Ambati, T. Gerasimov, L. De Lorenzis, A review on phase-field models of brittle fracture and a new fast hybrid formulation, Computational Mechanics 55 (2) (2015) 383–405.
[45] T. Gerasimov, L. De Lorenzis, A line search assisted monolithic approach for phase-field computing of brittle fracture, Computer Methods in Applied Mechanics and Engineering 312 (2016) 276–303.
[46] R. Romani, M. Bornert, D. Leguillon, R. Le Roy, K. Sab, Detection of crack onset in double cleavage drilled specimens of plaster under compression by digital image correlation–theoretical predictions based on a coupled criterion, European Journal of Mechanics-A/Solids 51 (2015) 172–182.
[47] E. G. Kirsch, Die theorie der elastizit t und die bed rfnisse der festigkeitslehre, Zeitshrift des Vereines deutscher Ingenieure 42 (1898) 797–807.
[48] M. Strobl, T. Seelig, On constitutive assumptions in phase field approaches to brittle fracture, Procedia Structural Integrity 2 (2016) 3705–3712.
[49] P. K. Kristensen, E. Martínez-Pañeda, Phase field fracture modelling using quasi-newton methods and a new adaptive step scheme, Theoretical and Applied Fracture Mechanics 107 (2020) 102446.
[50] E. Sacco, Modellazione e calcolo di strutture in materiale non resistente a trazione, Atti della Accademia Nazionale dei Lincei. Classe di Scienze Fisiche, Matematiche e Naturali. Rendiconti Lincei. Matematica e Applicazioni 1 (3) (1990) 235–258.